J. Fluid Mech. (2014), *vol.* 749, *pp.* 227–274.
doi:10.1017/jfm.2014.170

Evolution of the scalar dissipation rate downstream of a concentrated line source in turbulent channel flow

E. Germaine, L. Mydlarski† and L. Cortelezzi

Department of Mechanical Engineering, McGill University, Montréal, Québec, H3A 0C3, Canada

(Received 25 March 2013; revised 6 March 2014; accepted 26 March 2014;
first published online 15 May 2014)

The dissipation rate, ε_θ, of a passive scalar (temperature in air) emitted from a concentrated source into a fully developed high-aspect-ratio turbulent channel flow is studied. The goal of the present work is to investigate the return to isotropy of the scalar field when the scalar is injected in a highly anisotropic manner into an inhomogeneous turbulent flow at small scales. Both experiments and direct numerical simulations (DNS) were used to study the downstream evolution of ε_θ for scalar fields generated by line sources located at the channel centreline ($y_s/h = 1.0$) and near the wall ($y_s/h = 0.17$). The temperature fluctuations and temperature derivatives were measured by means of a pair of parallel cold-wire thermometers in a flow at $Re_\tau = 520$. The DNS were performed at $Re_\tau = 190$ using a spectral method to solve the continuity and Navier–Stokes equations, and a flux integral method (Germaine, Mydlarski & Cortelezzi, *J. Comput. Phys.*, vol. 174, 2001, pp. 614–648) for the advection–diffusion equation. The statistics of the scalar field computed from both experimental and numerical data were found to be in good agreement, with certain discrepancies that were attributable to the difference in the Reynolds numbers of the two flows. A return to isotropy of the small scales was never perfectly observed in any region of the channel for the downstream distances studied herein. However, a continuous decay of the small-scale anisotropy was observed for the scalar field generated by the centreline line source in both the experiments and DNS. The scalar mixing was found to be more rapid in the near-wall region, where the experimental results exhibited low levels of small-scale anisotropy. However, the DNS, which were performed at lower Re_τ, showed that persistent anisotropy can also exist near the wall, independently of the downstream location. The role of the mean velocity gradient in the production of ε_θ (and therefore anisotropy) in the near-wall region was highlighted.

Key words: mixing, turbulent mixing

1. Introduction

The ability of turbulence to mix one or more scalars within a fluid is of particular relevance to a variety of engineering applications including combustion, pollution dispersion and heat transfer. Using premixed combustion as an example, reactions

† Email address for correspondence: laurent.mydlarski@mcgill.ca

occur only if the fuel and oxidizer are sufficiently mixed at the molecular level prior to ignition. However, our comprehension and ability to predict turbulent mixing are limited because the fluid mechanics that governs turbulent mixing involves multiscale phenomena for which the details are not yet fully understood.

The turbulent mixing process stretches and stirs the scalar field, which serves to increase the scalar gradients. The scalar fluctuations are then smoothed out by the molecular mixing that principally occurs at the smallest scales of the turbulence. The rate of destruction of the scalar variance is quantified by the scalar dissipation rate, $\varepsilon_\theta (\equiv \alpha \langle (\partial\theta/\partial x_i)^2 \rangle)$. It is the only term in the scalar variance budget that must be non-zero in every turbulent flow. Consequently, ε_θ is omnipresent and of critical importance to the description of turbulent scalar fields. Furthermore, it is a quantity whose primary contributions derive from the smallest scales of the scalar field.

The predominant theory related to turbulent scalar mixing, Kolmogorov–Obukhov–Corrsin (KOC) theory, predicts that the small scales should be isotropic and independent of the large scales of a scalar field, the latter being anisotropic in most cases. However, it has been shown that departure from isotropy occurs at the small scales of the scalar field when its large scales are anisotropic, which questions KOC phenomenology (Warhaft 2000).

Investigations into the local isotropy of the scalar field (and, in particular, violations thereof) have been widely reported in the literature (e.g. Sreenivasan 1991). However, a large majority of these studies have focused on the evolution of a scalar field injected into a homogeneous and isotropic turbulent hydrodynamic field at large scales. While the assumption of homogeneity considerably simplifies the analysis and yields interesting similarities between the scaling of the velocity and scalar fields when the injection occurs at large scales (Corrsin 1952; LaRue & Libby 1981; Ma & Warhaft 1986; Danaila, Antonia & Burattini 2012), such a configuration is not representative of real flows, which are generally inhomogeneous and exhibit discrepancies between the scales of the velocity and scalar fields. Furthermore, only a small subset of previous work has focused on the dissipation rate of the scalar variance, even though ε_θ remains one of the less understood (yet most important) quantities within a turbulent flow.

The small-scale injection of a scalar by means of a point or line source into an inhomogeneous flow is of relevance to multiple engineering applications, including the transport of a plume emitted by a smokestack in the atmospheric boundary layer or the mixing of chemical species injected into a combustion chamber. Given the importance of such applications, it is somewhat surprising that relatively few studies of turbulent scalar mixing resulting from small-scale injection and focusing on the scalar dissipation rate, ε_θ, have been undertaken. This fact motivates the research herein.

The main objective of the present work is to further investigate and understand the evolution of the scalar field when injected in a highly anisotropic manner at small scales into an inhomogeneous turbulent flow. In measuring the evolution of ε_θ downstream of the source, we aim to further our understanding of the details of the scalar mixing process, which will improve our effectiveness in predicting the phenomena that rely on this process. In many cases, local isotropy is invoked when estimating ε_θ. When the scalar is injected at small scales, such an assumption is clearly inaccurate near the source. Furthermore, although this assumption may increase in validity with increasing distance from the source, the rate at which it does so is an important factor. Therefore, particular attention will be paid to the evolution of the three different components of the scalar dissipation rate, $\varepsilon_{\theta_x} \equiv \alpha \langle (\partial\theta/\partial x)^2 \rangle$, $\varepsilon_{\theta_y} \equiv \alpha \langle (\partial\theta/\partial y)^2 \rangle$ and $\varepsilon_{\theta_z} \equiv \alpha \langle (\partial\theta/\partial z)^2 \rangle$. We focus our attention on the relative contributions

of ε_{θ_x}, ε_{θ_y} and ε_{θ_z} to ε_θ, and therefore on the evolution of this anisotropy. To this end, all three components of the scalar dissipation rate have been studied both experimentally and by means of numerical simulations.

The remainder of this paper is organized as follows. The relevant literature is reviewed in § 2. Then, the experimental apparatus and details of the numerical simulations are reported, respectively, in §§ 3 and 4. Results are presented in §§ 5–7, comparing, as often as possible, the experimental and numerical results. The first of these three sections presents results pertaining to the velocity field. The second presents large-scale statistics (mean and root-mean-square (r.m.s.) temperatures) and compares them with the previous results of Lavertu & Mydlarski (2005) to validate the present measurements. Section 7, which comprises the vast majority of the results presented herein, reports in detail the evolution of the scalar dissipation rate and its three components at several locations. Finally, conclusions are presented in § 8.

2. Literature review

The theoretical foundation of (hydrodynamic) turbulence was proposed by Kolmogorov (1941). This work, commonly referred to as K41, introduces several concepts necessary for the description of the transport and dissipation of turbulent kinetic energy in a turbulent flow. As there is also significant interest in heat and mass transfer, Kolmogorov's arguments were extended by Obukhov (1949) and Corrsin (1951) to the transport of passive scalars, referred to as KOC phenomenology. At sufficiently high Reynolds numbers ($Re = UL/\nu$, where U is an average fluid velocity, L is some characteristic length of the system and ν is the kinematic viscosity of the fluid) and Péclet numbers ($Pe = UL/\alpha$ or UL/D, where α is the thermal diffusivity of the fluid and D is the scalar (molecular) diffusivity of a chemical species in the fluid), it supposes that there is a decay of any large-scale anisotropy when smaller and smaller scales are considered, the scalar dissipative scales returning to a statistically isotropic state. The smallest hydrodynamic and scalar scales (η and η_θ, respectively) are related by the Prandtl number ($Pr = \nu/\alpha$) or Schmidt number ($Sc = \nu/D$). (Subsequently, in the interest of conciseness, we will assume that the scalar under consideration is temperature in our discussions.) The relationship between η, η_θ and Pr depends on whether $Pr > 1$ or $Pr < 1$. It should be noted that η_θ and η are of the same order of magnitude in the air flow studied herein, where $Pr = 0.7 \approx O(1)$. Therefore $\eta_\theta = \eta Pr^{-3/4}$ (Corrsin 1951), where $\eta = (\nu^3/\varepsilon)^{1/4}$ and where $\varepsilon \equiv 2\nu\langle s_{ij}s_{ij}\rangle$ is the dissipation rate of turbulent kinetic energy. Here, $s_{ij} \equiv \frac{1}{2}(\partial u_i/\partial x_j + \partial u_j/\partial x_i)$ is the fluctuating strain rate.

The transport of a scalar quantity injected by a line source into a turbulent flow has been studied since the early experiments of Taylor (1935) and Uberoi & Corrsin (1952). Measurements taken downstream of a heated line source in homogeneous isotropic turbulence were carried out by Warhaft (1984) and Stapountzis *et al.* (1986). The authors showed that, in isotropic turbulence, the development of the mean thermal wake can be divided into three stages corresponding to different times t: (i) a molecular diffusive range ($t \ll \alpha/\langle v^2\rangle$, where $\langle v^2\rangle$ is the velocity variance in the transverse direction), in which the width of the mean temperature profile, σ_{mean}, increases as $\sqrt{t}$, (ii) a turbulent convective range ($\alpha/\langle v^2\rangle \ll t \ll t_L$, where t_L is the Lagrangian integral time scale) in which the growth of σ_{mean} is linear in time and (iii) a turbulent diffusive range ($t \gg t_L$) where σ_{mean} is proportional to $t^{(2-n)/2}$ ($n \approx 1$ is the decay exponent of the velocity field). Subsequently, Karnik & Tavoularis (1989) investigated the evolution of a thermal plume in a homogeneous (but non-isotropic)

turbulent shear flow. In contrast with grid turbulence, there is a continuous supply of kinetic energy from the mean shear to the turbulence, ensuring that the turbulence does not decay in this flow. The authors observed that the decay of the scalar fluctuations close to the source was not very different from that observed in isotropic turbulence. However, farther downstream, the mean shear affected the scalar statistics, imposing the effect of its large-scale anisotropy on the evolution of the scalar. Chung & Kyong (1989) also investigated the dispersion of a turbulent temperature field behind a line source in a homogeneous turbulent shear flow. Their goal was to provide experimental data for the assessment of third-order transport models. The mean and r.m.s. scalar profiles were found to exhibit nearly Gaussian distributions except for a minor degradation in the central region of the r.m.s. temperature profile. The evolution of second-order moments of scalar plumes, emitted from instantaneous and continuous area, line and point sources, was modelled by Thomson (1996). Given that the flow under consideration was homogeneous isotropic turbulence, he was also able to model the evolution of the scalar dissipation rate (via the scalar variance budget). Livescu, Jaberi & Madnia (2000) used direct numerical simulations (DNS) to study the development of the scalar plume produced by a line source in decaying homogeneous isotropic turbulence. Their study focused on a statistical analysis of moments of different orders and confirmed the experimental results of Warhaft (1984).

Although previous work on homogeneous flows has notably increased our understanding of the mixing of scalars emitted from sources at small scales, their applicability to engineering and natural flows remains somewhat limited given that almost all 'real' flows (e.g. jets, boundary layers, duct flows) are inhomogeneous. Consequently, scalar dispersion within inhomogeneous flows has also been studied. To this end, Fackrell & Robins (1982) investigated the evolution of a thermal plume emitted from a point source in a turbulent boundary layer. The authors reported measurements of the variance, intermittency, peak concentration values, probability density function (p.d.f.) and spectra of the scalar field. They showed that most of the fluctuations are produced in the vicinity of the source, and that the maximum amplitude of the fluctuations is source-size-dependent. Raupach & Legg (1983) studied the dispersion of a thermal plume emitted in a turbulent boundary layer from a line source. Their work was focused on testing first- and second-order closure models. To this end, they measured the dissipation rate of the temperature fluctuations by assuming local isotropy and using Taylor's hypothesis ($\varepsilon_{\theta iso} \approx (3\alpha/\langle U\rangle^2)\langle(\partial\theta/\partial t)^2\rangle$, where angular brackets represent averaged quantities). They reported that their measurements of ε_θ were 20 % below its value inferred from the scalar variance budget. Paranthoën *et al.* (1988) studied the evolution of the temperature field downstream of a line source in a turbulent boundary layer and in a planar jet. They reported mean and r.m.s. profiles of the temperature field and proposed a rescaling scheme based on the temporal integral Lagrangian scale of the vertical velocity fluctuations. The scheme was shown to be efficient in rescaling the mean profiles, but not the r.m.s. profiles. Tong & Warhaft (1995) studied the dispersion and mixing of temperature fluctuations emitted in the self-similar region of an axisymmetric turbulent jet from two heated annular (ring) sources. The two sources were used to study the mixing of two independently introduced scalar fields. Their results contrasted with those obtained in grid turbulence (Warhaft 1984), where the mixing and dispersion were slower. The authors also showed that far downstream of the jet exit, the scalar field becomes independent of its method of introduction into the flow. Tong & Warhaft (1995) also examined the relationship between the integral-scale and dissipation-scale fluctuations in the far-field. Even though they reported that

large- (θ^2) and small-scale ($\Delta\theta^2$) quantities become less coupled as the Reynolds number increases, the conditional expectations of $\Delta\theta^2$ on θ exhibited a significant dependence of the former on the latter. Rosset *et al.* (2001) investigated the transport of temperature behind a line source in a turbulent jet and a turbulent boundary layer over a flat plate. The authors were particularly interested in the behaviour of the scalar dissipation rate, ε_θ. Near the source, they observed a large anisotropy of the dissipative scales, which was explained by the high temperature gradient imposed by the source and by the flapping of the thermal wake. This anisotropy persisted downstream in the off-centre region of the plume. However, in the central part of the plume, they reported a return to isotropy of the different components of ε_θ. Rosset *et al.* (2001) derived a model to estimate the return-to-isotropy time scale and proposed arguments to explain this phenomenon. Nevertheless, they ultimately remarked that the details of the process remain to be understood.

One subset of inhomogeneous flows is of particular interest. Fully developed turbulent duct flows, of circular or high-aspect-ratio cross-section, are only inhomogeneous in one (the wall-normal) direction. Such a characteristic simplifies the analysis given that the inhomogeneity of the underlying velocity field is limited to one direction (as opposed to two or three). Brethouwer *et al.* (1999) used DNS to study the turbulent mixing of a passive scalar in fully developed turbulent pipe flow. In their work, the scalar was released from a point source at the centreline of the pipe. They presented large-scale statistics, i.e. mean and r.m.s. concentration profiles, turbulent fluxes and p.d.f.s which, in this case, at the centre of the flow, compared favorably with experimental data from grid turbulence. The release of a scalar field from a line source in a turbulent channel flow has also been investigated in the experiments of Lavertu & Mydlarski (2005). The authors studied the evolution of the temperature field in turbulent channel flow. The line source was oriented in the spanwise (z) direction, resulting in a thermal plume that was statistically two-dimensional. The authors reported large-scale statistics measured at different downstream locations in the scalar plume and for several wall-normal locations of the line source. They observed significant differences from the results in grid turbulence, which were attributed to the inhomogeneity of this flow in the wall-normal direction. Vrieling & Nieuwstadt (2003) and Costa-Patry & Mydlarski (2008) both studied the passive scalar mixing downstream of two line sources in fully developed turbulent channel flow using DNS and experiments, respectively. They showed that mean temperature values can be inferred from measurements downstream of a single source. However, the combined variance of two sources cannot be obtained by adding the variances of the individual sources. In contrast to Lavertu & Mydlarski (2005) and Costa-Patry & Mydlarski (2008), Bakosi, Franzese & Boybeyi (2007) used p.d.f. methods and the interaction by exchange with the conditional mean (IECM) model to investigate the dispersion of a passive scalar released continuously from a concentrated source in a turbulent channel flow. The one-point statistics of the scalar field were compared with the DNS data of Abe, Kawamura & Matsuo (2004) and the experimental data of Lavertu & Mydlarski (2005). The widths of the mean scalar profiles obtained with the IECM model were larger than those measured in the experiments at different downstream locations from the source. Boppana, Xie & Castro (2012) performed large-eddy simulations (LES) of the dispersion of a scalar from a line source in a turbulent channel flow. They reported mean and r.m.s. profiles and p.d.f.s of the scalar fluctuations. Their results were also compared with the experiments of Lavertu & Mydlarski (2005), which exhibited discrepancies for both the width and location of the peak of the profile. It should be noted that in contrast to Bakosi *et al.* (2007),

the widths of the mean profile computed by Boppana *et al.* (2012) were smaller than those obtained from Lavertu's experiments. In addition, Boppana *et al.* (2012) observed a double peak in the r.m.s. profiles at locations downstream from the source ($x/h > 7.4$) that were not reported in the experiments. The p.d.f.s of both the LES and experiments were in good agreement, apart from the thermal fields generated by the centreline source. Lepore & Mydlarski (2011) studied the downstream evolution of a three-dimensional thermal plume in the turbulent channel flow released by a line source oriented in the wall-normal direction. They examined in detail the mean and fluctuating temperature fields at different locations in the thermal plume to highlight the differences between lateral and transverse dispersion. Lastly, Mydlarski, Danaila & Lavertu (2007) focused on the dissipation rate of a scalar field emitted from a line source in a turbulent channel flow. The authors confirmed that small-scale anisotropy is amplified at the interfaces between the plume and the ambient fluid. They reported that a large anisotropy occurs in regions of high turbulent intensity and their results showed that there may exist a competition between mechanisms that amplify and destroy anisotropy. However, ε_θ was not directly measured in this work, but was inferred from the scalar variance budget (given certain assumptions). In contrast to their work, the present work directly measures (all three components of) the scalar dissipation rate, using both experiments and numerical simulations.

3. Experimental apparatus

The experiments were conducted in the same open-circuit channel as the one used by Lavertu & Mydlarski (2005), Costa-Patry & Mydlarski (2008) and Lepore & Mydlarski (2011). The air flow was supplied by a Hudson Buffalo centrifugal blower powered by a 7.5 h.p. electric motor whose speed was monitored by an ABB ACS 600 controller. The air flow was filtered at the inlet of the motor to prevent particles (of diameter greater than 3 μm) from entering the channel. A flexible rubber coupling was used to join the blower output to the entrance of the flow conditioning section to minimize the transmission of any blower vibrations to the flow conditioning section. The latter consisted of a wide-angle diffuser, a settling chamber and a contraction. After exiting the contraction, the flow that entered the channel was uniform and had a low turbulence intensity (0.25 %).

The test section was 8 m long and had a large aspect ratio, i.e. the height of the channel in the spanwise (z) direction was large (1.1 m) compared with its width ($2h = 0.06$ m) in the wall-normal (y) direction, see figure 1. Consequently, the flow was statistically independent of z, away from the top and bottom walls of the channel. The development of the flow was accelerated by the addition of two 3 mm diameter cylindrical rods (located 3 mm from each wall, at the entrance of the test section) that tripped the boundary layers that formed on the test section walls. At the downstream end of the test section, where the measurements were recorded, the flow was fully developed with a mean flow in the downstream (x) direction and zero mean wall-normal (V) and lateral (W) velocities. In the fully developed region, the flow was statistically stationary and one-dimensional with velocity statistics depending only on the wall-normal distance (y). It should be noted that such a flow is statistically symmetric about the midplane. Lastly, 7.5 cm of honeycomb mesh (of 5 mm cell size) was used at the outlet to prevent perturbations from outside the channel from being communicated upstream, into the channel. The flow conditions are listed in table 1.

In the test section, the scalar (temperature) was injected into the flow by heating a fine line source. The latter was a 0.127 mm diameter Ni–Cr wire extended across the

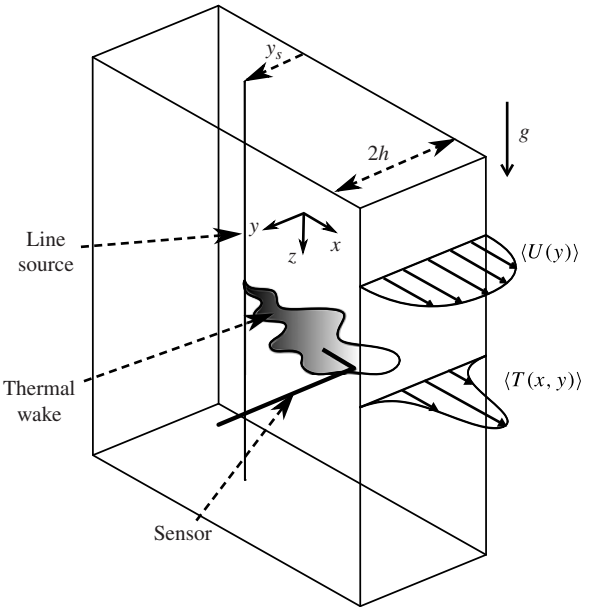

FIGURE 1. Schematic of the experiment. Adapted from Lepore & Mydlarski (2011).

	Exp.	DNS
$\langle U\rangle_{y/h=1}$ (m s^{-1})	5.3	—
$u_{rms_{y/h=1}}$ (m s^{-1})	0.22	—
u_τ (m s^{-1})	0.26	—
$\eta_{y/h=1}$ (m)	0.28×10^{-3}	—
Re $(=\langle U\rangle_{y/h=1}h/\nu)$	10 600	3600
Re_τ $(=u_\tau h/\nu)$	520	190
Re_λ $(=u_{rms_{y/h=1}}\lambda_{y/h=1}/\nu)$	59	36
$y_s/h=0.17$	$y_s^+=88$	$y_s^+=33$
$y_s/h=1.0$	$y_s^+=520$	$y_s^+=190$

TABLE 1. Flow parameters. Properties of the flow considered in the experiments and numerical simulations, and source locations in terms of wall units. Here, $\nu = 15 \times 10^{-6}$ m^2 s^{-1}.

spanwise direction of the test section at wall-normal locations of $y_s/h = 1.0$ (channel centreline) and $y_s/h = 0.17$ (near-wall region). The wire was heated electrically by a DC power supply and the power consumption was continuously monitored so that the energy released into the flow remained equal to 45 W m^{-1}. See figure 1 for a schematic of the experiment.

The temperature fluctuations, θ, and their dissipation rate, ε_θ, were measured by means of cold-wire thermometry. The sensors were inserted into the channel from its outlet using a (915 mm-long) probe support (TSI-1155-36). Accurate positioning of the sensor in the wall-normal direction was ensured by means of a precision transversing mechanism driven by a computer-controlled stepper motor. The minimum step increment was 0.01 mm. The sensor consisted of two parallel 90 % platinum/10 % rhodium wires of 0.63 μm diameter mounted on a TSI 1244 probe. The variations

of the sensor temperature were linearly proportional to its electrical resistance (over small ranges) and were measured by a cold-wire thermometry circuit designed by Lemay & Benaïssa (2001). The output signals of the cold-wire thermometer were (i) amplified and filtered by a Krohn-Hite 3384 eight-pole filter and (ii) digitized using a 16 bit (±5 V) National Instruments PCI 6036E data acquisition card. The acquisition procedure was undertaken using LabVIEW virtual instruments. Depending on the wall-normal location of the probe, the sampling frequency (2.5 times the low-pass filter frequency) was in the range 5–10 kHz andthe sampling time was fixed at 200 s for each location. The length-to-diameter ratio of the cold-wire sensors was approximately 800 (i.e. $l_{wire} \approx 0.5$ mm) and their frequency response was approximately 5 kHz when operated in a 5 m s^{-1} flow. It should be noted that the temporal resolution of the wire was sufficient given that the Kolmogorov frequencies, $f_\eta = \langle U \rangle / (2\pi\eta)$, of the flow studied herein did not exceed 4 kHz. In addition, the (temporal resolution) correction proposed by Lemay & Benaïssa (2001) was applied to the acquired data. However, the effect of this correction was relatively small as it increased the estimate of the temperature dissipation by less than 1 % when measured at the farthest downstream location and by 5 % when measured at the location closest to the line source.

The scalar derivative $(\partial\theta/\partial x)$ in the downstream direction was estimated using Taylor's hypothesis in conjunction with the time derivative of the temperature $(\partial\theta/\partial t)$. This measurement required only a single cold wire, whereas two wires were needed to estimate the derivatives $\partial\theta/\partial y$ and $\partial\theta/\partial z$ in the wall-normal and spanwise directions, respectively. Zhou *et al.* (2003) investigated the effects of the separation between the two wires and found that the spectra of the temperature derivatives are significantly affected by the electronic noise contamination from one wire to the other when the separation is smaller than 3η. In addition, they recommended the use of a correction method similar to that of Wyngaard (1969) when the wire separation was larger than 3η. As a consequence, we designed our sensors so that the separation between the two wires was nominally 3η ($= 0.75$ mm), which was slightly smaller than 3η at the channel centreline and slightly larger near the wall, as η is a function of the wall-normal position. This conclusion is furthermore supported by the works of Antonia & Mi (1993), Anselmet, Djeridi & Fulachier (1997) and Danaila *et al.* (2000), who all agree that wire separations of 3η are optimal.

4. Numerical simulations

To complement the experiments described in § 3 and provide further insight into the evolution of the scalar dissipation rate, we performed DNS of a nearly identical problem. The fully developed turbulent flow can be assumed to be homogeneous in the spanwise and streamwise directions while the scalar field can be assumed to be homogeneous in the spanwise direction only. The scalar field presents a sharp gradient at the line source while the velocity gradients of the hydrodynamic field are smooth. However, since the temperature difference between the fluid in the plume and the incoming fluid is small, the hydrodynamic problem can be assumed to be one-way coupled with the advection–diffusion problem. Therefore, we split the DNS into two parts: we first compute the solution to the hydrodynamic field and, subsequently, the solution to the advection–diffusion problem.

Spectral methods have become a standard tool to simulate fully developed turbulent channel flows because of their high accuracy and kinetic energy conservation properties. We directly numerically simulate the time evolution of the hydrodynamic

flow field by solving continuity and Navier–Stokes equations,

$$\frac{\partial U_i}{\partial x_i} = 0, \quad \frac{\partial U_i}{\partial t} + U_j \frac{\partial U_i}{\partial x_j} = -\frac{1}{\rho}\frac{\partial p}{\partial x_i} + \nu \frac{\partial^2 U_i}{\partial x_j \partial x_j}, \tag{4.1}$$

with periodic boundary conditions in the streamwise (x) and spanwise (z) directions, and no-penetration and no-slip conditions at the walls, see figure 1. The streamwise mean pressure gradient, which drives the mean flow in the x direction, is adjusted dynamically to maintain a constant mass flux through the channel. To integrate the above equations, we use the spectral code Channelflow (Gibson, Halcrow & Cvitanović 2008; Gibson 2010, licensed under the GNU GPL, http://channelflow.org/), which uses Fourier × Chebyshev × Fourier discretization in the x, y and z directions, and a third-order Runge–Kutta method for the time integration.

Spectral methods, however, are not suitable for the simulation of a scalar field injected by means of a line source, i.e. a singularity, that introduces a sharp gradient in the scalar field. In the presence of a sharp gradient, the convergence rate of spectral methods deteriorates to first order because spurious oscillations develop in the vicinity of a line source and propagate in the flow field (Gibbs phenomenon). Furthermore, spectral methods are not suited for the solution of non-periodic problems. (See, for example, Simens *et al.* 2009, for details.) Therefore, we solve the advection–diffusion equation

$$\frac{\partial T}{\partial t} + U_j \frac{\partial T}{\partial x_j} = \alpha \frac{\partial^2 T}{\partial x_j \partial x_j}, \tag{4.2}$$

with periodic boundary conditions in the spanwise (z) direction, inflow/outflow at the inlet/outlet of the channel and adiabatic (no-flux) at the walls (see figure 1) using a scheme we developed, named 3DFLUX (Germaine, Mydlarski & Cortelezzi 2013). 3DFLUX is a high-order three-dimensional conservative monotonicity preserving numerical solver. It is nominally third-order in space and second-order in time. The line source used in the experiment is simulated using a string of constant-source nodes located on a straight line, oriented parallel to the z-axis.

In this two-step numerical approach, the solenoidal velocity field of the turbulent channel flow is precomputed by the Channelflow code and, subsequently, passed as an input to the 3DFLUX code to solve the advection–diffusion equation. This passage, while apparently trivial, is indeed very delicate because of the different velocity representations and grids used in the two codes. In Channelflow, the velocity field has a spectral representation with a resolution dictated by the number of Fourier and Chebyshev modes used. In 3DFLUX, the computational domain is discretized with a number of non-overlapping control volumes or cells. The scalar field is discretized at the centre of each cell, whereas the components of the velocity field are stored at the centres of the faces of each cell (staggered grid). Therefore, the velocity field produced by Channelflow is passed to 3DFLUX by interpolating the spectral representation of the velocity field on each face of the 3DFLUX grid.

The interpolation of a divergence-free velocity field has been the subject of several publications in the last decade (see, for example, Balsara 2001; Li & Li 2004; Chamecki, Meneveau & Parlange 2008). The method proposed by Chamecki *et al.* (2008) is efficient only when the grids of the two different discretization methods are identical, and therefore is not applicable herein. We devised our own method in which we first used a spectral (exact) interpolation to compute the values of the velocity components at nine points on each face, i.e. one at the centre, four at the corners

	Velocity	Scalar $y_s/h = 1.0$	Scalar $y_s/h = 0.17$
$L_x \times L_y \times L_z$	$2\pi h \times 2h \times \pi h$	$2\pi h \times 2h \times \pi h$	$2\pi h \times 2h \times \pi h$
$L_x^+ \times L_y^+ \times L_z^+$	$1187 \times 378 \times 594$	$1187 \times 378 \times 594$	$1187 \times 378 \times 594$
$N_x \times N_y \times N_z$	$256 \times 193 \times 192$	$514 \times 195 \times 194$	$258 \times 390 \times 194$
Δx^+, Δy^+, Δz^+	4.64, 0.025–3.1, 3.1	2.32, 1.96, 3.1	4.64, 0.98, 3.1
Δx^*, Δy^*, Δz^* at $y/h = 1.0$	1.25, 0.83, 0.84	—	—
Δx^*, Δy^*, Δz^* at $y/h = 0.17$	2.40, 0.88, 1.60	—	—
$\Delta x^\bullet$, $\Delta y^\bullet$, $\Delta z^\bullet$ at $y/h = 1.0$	—	0.50, 0.42, 0.66	0.99, 0.21, 0.66
$\Delta x^\bullet$, $\Delta y^\bullet$, $\Delta z^\bullet$ at $y/h = 0.17$	—	0.95, 0.80, 1.27	1.91, 0.40, 1.27
t_{sam}^+	2770	665	665

TABLE 2. Details of the numerical grids for the computation of velocity and scalar fields with two different source locations. The superscript '+' indicates the normalization by the viscous length (ν/u_τ) or time (ν/u_τ^2) scale, and the superscripts '$*$' and '$\bullet$' are used for the normalization by the Kolmogorov (η) and Corrsin (η_θ) length scales, respectively, estimated at $y/h = 1.0$ and 0.17 as specified.

and four at the midsides of the edges of the faces. Then, we computed the value of each velocity component at the face of each cell by averaging the nine interpolated values. Finally, we applied a very small correction to the u-component of the velocity field to guarantee the exact divergence-free condition. It should be noted that (i) the choice of the u-component is arbitrary (it could have been the w-component) and (ii) this correction has a minuscule impact on the velocity field, as it modifies the interpolated instantaneous values of the u-component by less than 0.01 %.

The simulations of the velocity and scalar fields were both performed without turbulence models, by resolving the entire range of scales. The computational conditions are reported in table 2 for (i) the hydrodynamic field and (ii) the scalar field for two source locations ($y_s/h = 1.0$ and $y_s/h = 0.17$). These DNS require that the computational domain be large enough to capture the integral scales and the spatial resolution be small enough to resolve, as accurately as possible, the dissipative scales. The large scales are correctly represented when the two-point correlations in the streamwise and spanwise directions are zero, respectively, at the half-length and half-height of the domain (Kawamura *et al.* 1998; Moser, Kim & Mansour 1999). The domain size selected herein is the same as in Kawamura *et al.* (1998), Moser *et al.* (1999) and Schwertfirm & Manhart (2007). The Kolmogorov (i.e. smallest) length scale should ideally be resolved. However, it has been claimed that this requirement is often too stringent. Moin & Mahesh (1998) noted that the smallest resolved length scale is required to be of the order of η but not equal to η. They further reported that very good agreement of large-scale statistics can be obtained between DNS and experiments even though the Kolmogorov scales are not fully resolved in the simulation. Kawamura *et al.* (1998) validated the resolution of their simulations by showing substantial drop-offs in the one-dimensional energy spectra at high wavenumbers.

Traditionally, the goal of most experiments is to resolve all scales of size η or larger. This being said, recent work has taken advantage of the constantly increasing computational power to simulate turbulent scalar mixing at spatial resolutions finer than η. For example, Schumacher, Sreenivasan & Yeung (2005) studied the fine structures of homogeneous and isotropic turbulent scalar mixing using high-resolution simulations (with the grid spacing smaller than η by a factor of two). They showed

that when large fluctuations of ε exist, a spatial resolution based on η (defined using its average value) incorrectly predicts the small-scale statistics. Kozuka, Seki & Kawamura (2009) and Galantucci & Quadrio (2010) both performed DNS of turbulent scalar mixing in channel flows at high resolution. Galantucci & Quadrio (2010) carried out three DNS at increasing spatial resolutions that they labelled low, medium and high. The low resolution was comparable with the resolution of most wall-turbulence DNS performed to date (with passive scalars), whereas, in the high resolution simulations, all cell sizes were consistently smaller than η_w, the averaged Kolmogorov length scale evaluated at the wall. The spatial resolution denoted medium was midway between the other two resolutions. The authors reported several statistics pertaining to the rate of dissipation of the scalar field (mean, variance and p.d.f.s of ε_θ). They showed that the estimates of ε_θ can increase by 5 % when using the high or medium resolutions instead of the low one. The resolutions used for the simulations presented herein (see table 2) are comparable with the medium resolution used by Galantucci & Quadrio (2010). The accuracy of the chosen resolution as it pertains to the smallest scales in the flow will be subsequently confirmed when the normalized (one-dimensional) dissipation spectra for the simulations are shown to be capable of reproducing the dissipative scales measured in the experiments.

To compute the hydrodynamic field, uniform meshes were used in the x and z directions, whereas a non-uniform mesh (Chebyshev distribution) was adopted in the y direction. As shown in table 2, two different grids were used to discretize the scalar field, depending on the source location. When the source was at the centreline, i.e. $y_s/h = 1.0$, a quasi-homogeneous grid was used given that the scalar plume did not interact with the walls (for the downstream locations studied herein). When the source was near the wall ($y_s/h = 0.17$), the grid resolution was halved in the y direction to capture the smallest wall-normal fluctuations of the scalar field that occur in the vicinity of the walls. The spatial resolution (Δx, Δy, Δz) of the scalar field generated by the centreline source was, for either grid, smaller than or equal to the Corrsin scale. The spatial resolution of the scalar field generated by the near-wall source was, in the worst case, less than twice the Corrsin scale in the x direction. However, note that Δy is always smaller than the Corrsin scale.

Lastly, to study the evolution of the scalar field at locations farther downstream, we adopted a strategy that consisted of connecting several channels in series and computing the solution for the scalar field sequentially, i.e. the outflow of the first channel became the inflow of the second one, and so on. It should be noted that the hydrodynamic field is the same in all channels because of its periodic boundary conditions. In this paper, we limited our computation to two channels, i.e. $(x/h)_{max} = 2L_x/h$, where L_x is the length of one channel in the x direction.

5. Results: velocity field

To be consistent with Lavertu & Mydlarski (2005), the experiments were carried out (in the same experimental facility) at $Re_\tau = 520$. However, the simulations were performed at a lower Reynolds number ($Re_\tau = 190$) to resolve all scales while keeping the flow turbulent and the computational effort feasible. Mean velocity profiles in fully turbulent channel flow from both the experiments and DNS are plotted in figure 2(*a*) and compared with the numerical results of Moser *et al.* (1999) ($Re_\tau = 180$ and 590) and Abe, Kawamura & Matsuo (2001) ($Re_\tau = 180$ and 640). The experiments of Hussain & Reynolds (1975) ($Re_\tau = 640$) are also included for comparison. The mean velocity profile obtained from the present DNS is in very good agreement with those

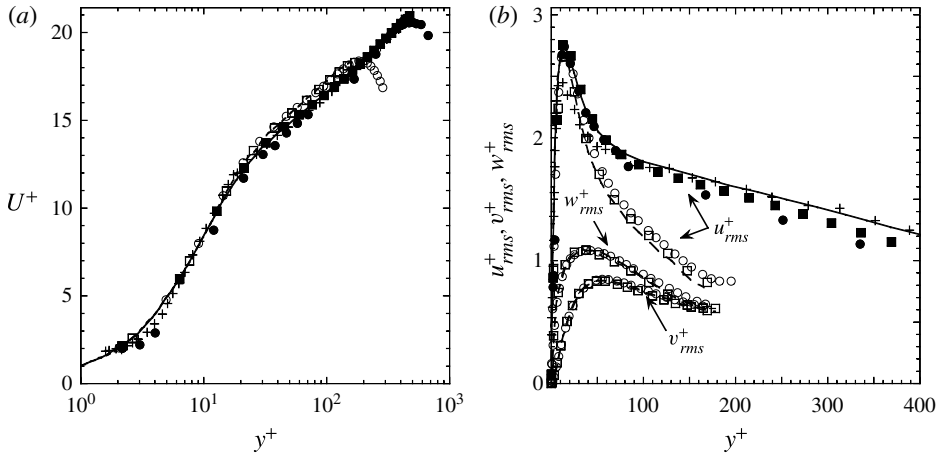

FIGURE 2. Velocity profiles in fully turbulent channel flow. Mean (*a*) and r.m.s. (*b*) velocity profiles (normalized by u_τ) from experiments ($Re_\tau = 520$ (●)), DNS ($Re_\tau = 190$ (○)) and compared with the DNS of Abe *et al.* (2001) ($Re_\tau = 180$ (- - -) and $Re_\tau = 640$ (—)) and Moser *et al.* (1999) ($Re_\tau = 180$ (□) and $Re_\tau = 590$ (■)), and the experiments of Hussain & Reynolds (1975) ($Re_\tau = 640$ (+)).

measured in flows at $Re_\tau = 180$. As noted by Kim, Moin & Moser (1987), even if $Re_\tau = 180$ is a relatively low Reynolds number (for a turbulent flow), both linear and logarithmic regions exist and are distinct. Small differences are observed between the experiments and the DNS. However, these differences can be attributed to the difference in Reynolds number of the flows, a conclusion that is confirmed by the good agreement between the present experimental results and the higher-Reynolds-number simulations of Moser *et al.* (1999) and Abe *et al.* (2001). These simulations also exhibit smaller values of u^+ for a given location y^+ in the logarithmic region.

The r.m.s. of the velocity fluctuations is plotted in figure 2(*b*). The data of Hussain & Reynolds (1975), Moser *et al.* (1999) and Abe *et al.* (2001) are once again reported for comparison, where available. The values of the three components (u^+_{rms}, v^+_{rms} and w^+_{rms}) increase with Re_τ and are consistent with the differences in the Reynolds number between the present experiments ($Re_\tau = 520$), Moser *et al.* (1999) ($Re_\tau = 590$) and Abe *et al.* (2001) ($Re_\tau = 640$). Furthermore, the present DNS ($Re_\tau = 190$) agrees very well with the results of Moser *et al.* (1999) and Abe *et al.* (2001) (both with $Re_\tau = 180$). In brief, figure 2(*b*) shows good agreement between the present and previous data obtained at similar Re_τ. (It should be noted that the peak value of u^+_{rms} measured by Hussain & Reynolds (1975) is somewhat low compared with the other results. This discrepancy may be justified by the difficulties in performing these early near-wall measurements.) Finally, it should be noted that the original and interpolated velocity fields are indistinguishable. Consequently only the former has been plotted.

6. Results: large-scale statistics of the scalar field

In this section, the large-scale statistics of the scalar field from experiments and numerical simulations are analysed and compared with those obtained in Lavertu & Mydlarski (2005). As the experiments were performed at a different Reynolds number from that of the numerical simulations, we normalized the downstream location (x/h) by the ratio $(u_{rms}/\langle U\rangle)^{-1}$, where u_{rms} and $\langle U\rangle$ are the r.m.s. and mean velocities

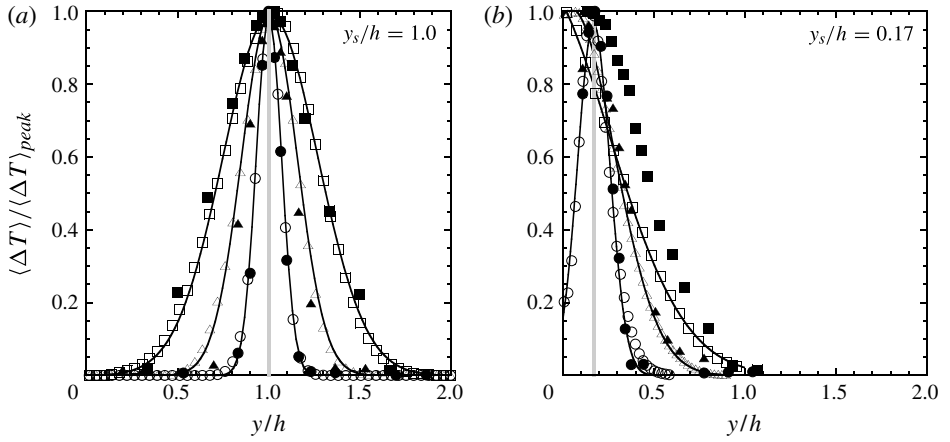

FIGURE 3. Non-dimensionalized mean temperature excess profiles for two line source locations. Experiments (solid symbols) and DNS (open symbols) are reported at several downstream locations: $t/t_L = 0.08$ (● and ○); $t/t_L = 0.2$ (▲ and △); $t/t_L = 0.4$ (■ and □). The vertical line indicates the transverse location of the source and the solid lines are the best-fit Gaussian curve fits to the numerical data.

measured at the centreline. It should be noted that this normalization is equivalent to normalizing the flight time from the source by (an approximation of) the integral time scale ($t_L \approx h/u_{rms}$),

$$t/t_L = \frac{(x/\langle U \rangle)}{(\ell/u_{rms})} \approx \frac{(x/\langle U \rangle)}{(h/u_{rms})} = \frac{(x/h)}{(\langle U \rangle/u_{rms})}. \tag{6.1}$$

The mean temperature profiles at three downstream locations behind the line source ($t/t_L = 0.08$, 0.2 and 0.4) are shown in figures 3(*a*) and 3(*b*) for the $y_s/h = 1.0$ and 0.17 source locations, respectively. Given that mean temperature excesses ($\langle \Delta T \rangle \equiv \langle T \rangle - T_\infty$) can be difficult to measure accurately due to drift in the free-stream temperature, we used the technique proposed by Lepore & Mydlarski (2011), which consists of sequentially measuring the free-stream (i.e. ambient, room) temperatures at the same location, immediately after measuring the mean temperatures at a given (x, y) location in the thermal plume, to estimate the mean temperature excess based on the 'instantaneous' free-stream temperature, which accounts for the aforementioned drifts in the free-stream temperature (as opposed to assuming that T_∞ is the same for all measurements of $\langle T(x, y) \rangle$).

For the centreline source location ($y_s/h = 1.0$), very good agreement between the experiments and numerical simulations is observed, and the mean profiles are well approximated by Gaussian curve fits. Gaussian fits are of interest for three reasons. First, a Gaussian profile is the analytical solution to the advection–diffusion equation for the dispersion from a line or point source in a constant velocity and constant, laminar or turbulent, diffusivity flow, which is approximately the case in the centre of the channel, and less so near the wall. Second, such fits assist in comparing with results that have been obtained in homogeneous turbulent flows, where Gaussian profiles have been observed. Third, due to the least-square fitting process, fitting a curve to the data allows a more precise estimate of the standard deviation (or, alternatively, the half-width) of the plume by reducing error. We further note that

the LES of Boppana *et al.* (2012), carried out at $Re_\tau = 520$ (i.e. the same value as the experiments herein), did not agree as well with the experiments of Lavertu & Mydlarski (2005) (which give very similar results to those herein and will be discussed shortly in the context of figures 5–8) and underestimated the plume width; see their figure 10(*c*). This presumably derives from their under-resolved transverse velocity fluctuations; they obtained values of $\langle v^2 \rangle$ at $y/h = 1$ that were 20 % lower than the those obtained by Moser *et al.* (1999) at $Re_\tau = 590$; see figure 5 in Boppana *et al.* (2012). Although a 20 % underestimate of $\langle v^2 \rangle$ may not seem egregious, the observed good agreement between the present DNS and experiments implies that accurate estimates of $\langle v^2 \rangle$ are critical to reliably predicting the evolution of the plume. We furthermore remark that the p.d.f. method simulations of Bakosi *et al.* (2007) overestimated the widths of the mean profiles for a centreline source. However, the explanation in this case is less clear, especially given that they also under-resolved $\langle v^2 \rangle$ (see their figure 1*b*), as noted by Boppana *et al.* (2012).

Similarly, good agreement between the experimental and numerical mean temperature profiles is obtained for the near-wall line source ($y_s/h = 0.17$). However, for the farthest downstream distance considered herein ($t/t_L = 0.4$) the experimental mean temperature profile is wider than the numerical one. Far downstream of the source, the (two-dimensional) plume grows and becomes wider in the transverse direction. One edge of the plume is mixed with the cold flow contained in the central region of the channel, whereas the other edge comes into contact with the (nominally) adiabatic walls. Consequently, the plume contains a hot region near the wall and a colder region away from the wall. The discrepancies observed for $t/t_L = 0.4$ in figure 3(*b*) are consistent with an energy loss (in the experiments) to the walls due to the latter not being perfectly adiabatic (because ΔT_{peak} is smaller than it should ideally be in the experiments due to the heat transfer from the plume to the wall). In dimensional terms, the peak mean excess temperature at $t/t_L = 0.4$ when $y_s/h = 0.17$ is less than 0.4 °C, so even very minor energy losses to the channel wall, which is not perfectly adiabatic in reality, can have an effect. For the case of the centreline source, neither side of the plume comes into contact with the channel walls and the mean temperature profile remains symmetric about the line source location, in very good agreement with the numerical simulations. Similarly to the case of the centreline source, the LES of Boppana *et al.* (2012) were found to underestimate the width of the mean plume when $y_s/h = 0.17$ at all downstream locations; see their figure 10(*b*). This presumably derives from their under-resolved transverse velocity fluctuations, combined with the abovementioned heat transfer to the wall in the experiments, which results in overly wide (normalized) plume widths further downstream.

The simulations also exhibit a shift in the peak of the mean profile towards the region of lower velocity (i.e. towards the wall) when $y_s/h = 0.17$. A similar shift was reported in Karnik & Tavoularis (1989). At the wall, the simulated mean temperature profiles must all exhibit $\partial \langle T \rangle / \partial y|_{y=0} = 0$, consistent with the adiabatic boundary conditions imposed in our simulations. Experimental measurements in the range $0 < y/h < 0.1$ were, however, not possible due to interference of the probe with the wall.

The transverse profiles of the r.m.s. temperature fluctuations, θ_{rms}, normalized by their peak values, $\theta_{rms\text{-}peak}$, are reported in figures 4(*a*) and 4(*b*) respectively for $y_s/h = 1.0$ and 0.17 at three downstream locations, $t/t_L = 0.08$, 0.2 and 0.4. The experimental and numerical results collapse well for both line source locations, in addition to being well approximated by Gaussian curve fits. At $y_s/h = 1.0$, the peaks of the fluctuations remain behind the line source, as expected, due to the underlying symmetry of this flow. However, for $y_s/h = 0.17$, a drift of the peak towards the

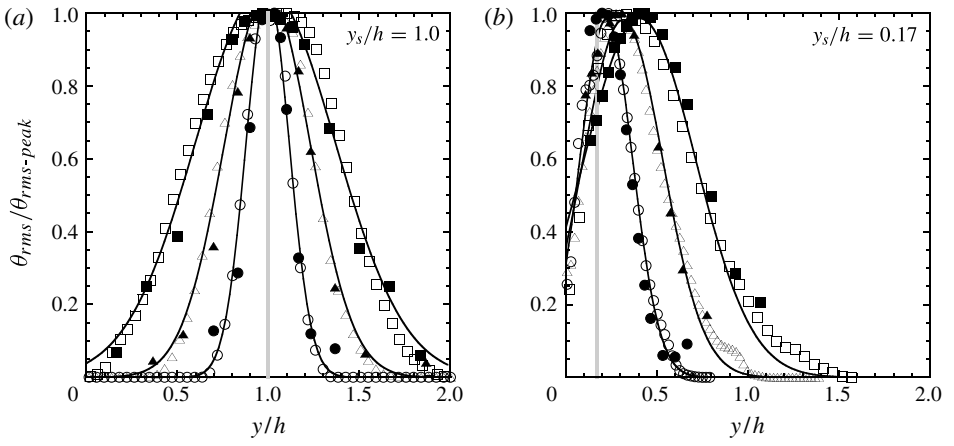

FIGURE 4. Non-dimensionalized r.m.s. temperature excess profiles for two line source locations. Experiments (solid symbols) and DNS (open symbols) are reported at several downstream locations: $t/t_L = 0.08$ (● and ○); $t/t_L = 0.2$ (▲ and △); $t/t_L = 0.4$ (■ and □). The vertical line indicates the transverse location of the source and the solid lines are the best-fit Gaussian curve fits to the numerical data.

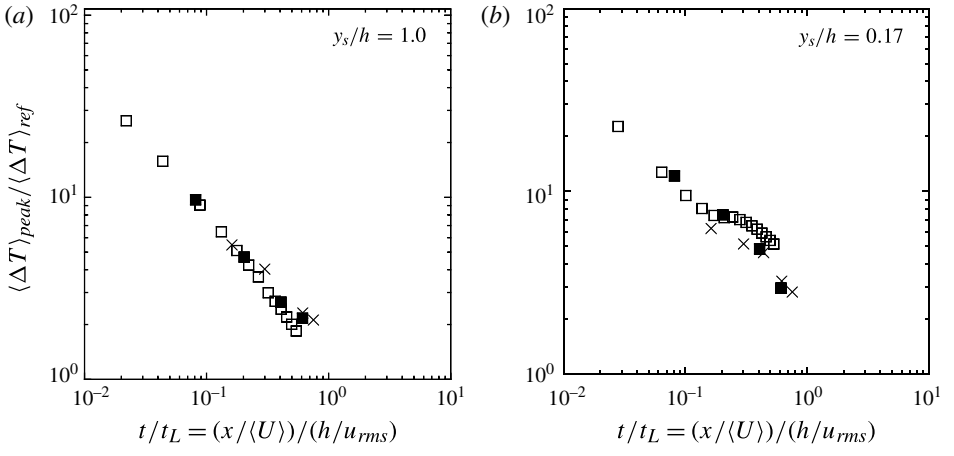

FIGURE 5. Downstream evolution of the non-dimensionalized peak mean temperature for two line source locations. Experiments (■), DNS (□) and Lavertu & Mydlarski (2005) (×).

centreline is clearly observed. Similar drifts have been reported in Fackrell & Robins (1982), Raupach & Legg (1983) and Lavertu & Mydlarski (2005). One should also note the very good agreement between the experiments and simulations at $t/t_L = 0.4$ for the case of the near-wall source. The good collapse of the two r.m.s. profiles (when normalized by their peak values) reaffirms our hypothesis that the disagreement observed in figure 3(*b*) for the mean profiles at the same location arises from an underestimate of ΔT_{peak}. For a centreline source, the LES of Boppana *et al.* (2012) underestimate the plume width, similarly to their results for the mean profile. For the case of the source at $y_s/h = 0.17$, the r.m.s. profiles of Boppana *et al.* (2012) are of a similar shape, but are offset and closer to the wall. Given that the r.m.s. profiles

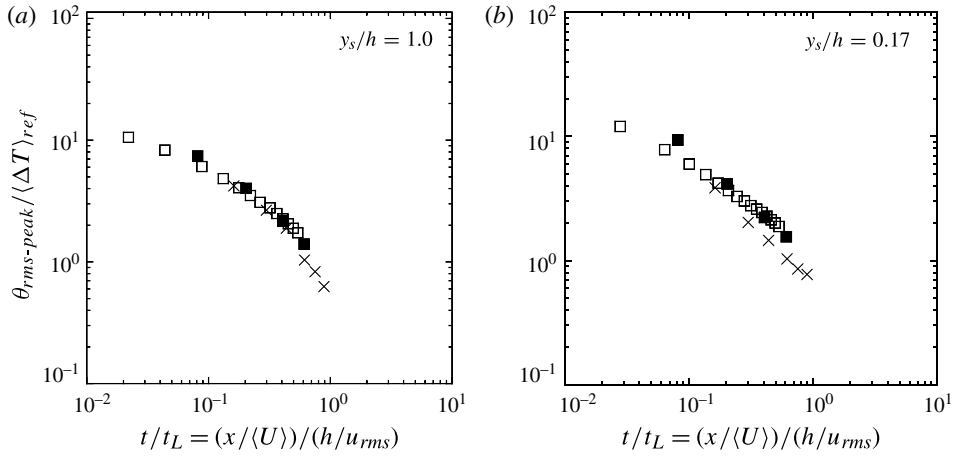

FIGURE 6. Downstream evolution of the non-dimensionalized peak r.m.s. temperature for two line source locations. Experiments (■), DNS (□) and Lavertu & Mydlarski (2005) (×).

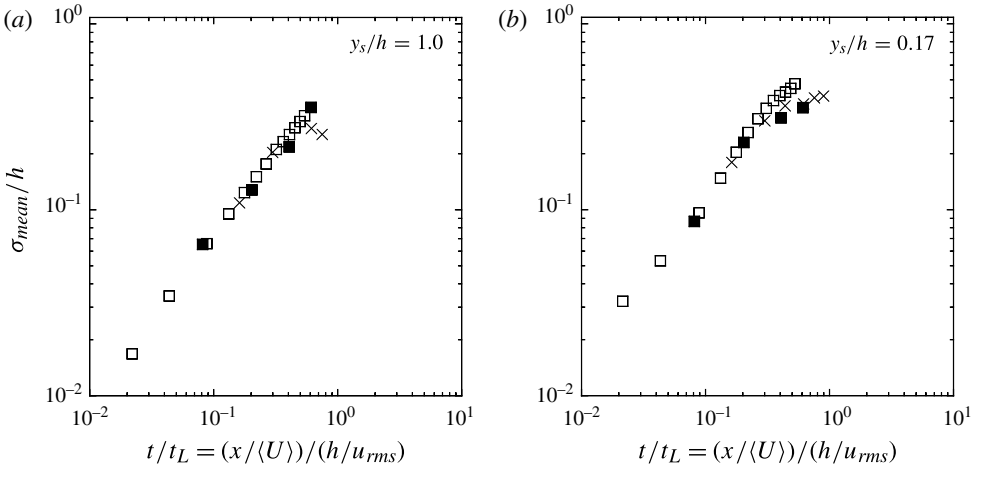

FIGURE 7. Downstream evolution of the non-dimensionalized width of the mean temperature profiles for two line source locations. Experiments (■), DNS (□) and Lavertu & Mydlarski (2005) (×).

are related to the mean profiles (i.e. the former can be predicted from the latter using gradient transport theory, for example), such a result is consistent with their mean profiles which are not as wide. Similarly to the mean profiles, the simulations of Bakosi *et al.* (2007) overpredicted the widths of the r.m.s. profiles.

The double-peaked r.m.s. profile in the vicinity of the source reported by Warhaft (1984) and Karnik & Tavoularis (1989) for homogeneous flows is also observed for the simulations (not shown). The double peak remains up to $t/t_L = 0.1$ $(x/h = 2.0)$, after which the profile becomes single-peaked. It should be noted that when $y_s/h = 0.17$ the double peak is not symmetric, as it must be for the centreline source case, with the near-wall peak having a lower magnitude. Lastly, note that experiments were not performed close enough to the line source to observe double-peaked θ_{rms} profiles.

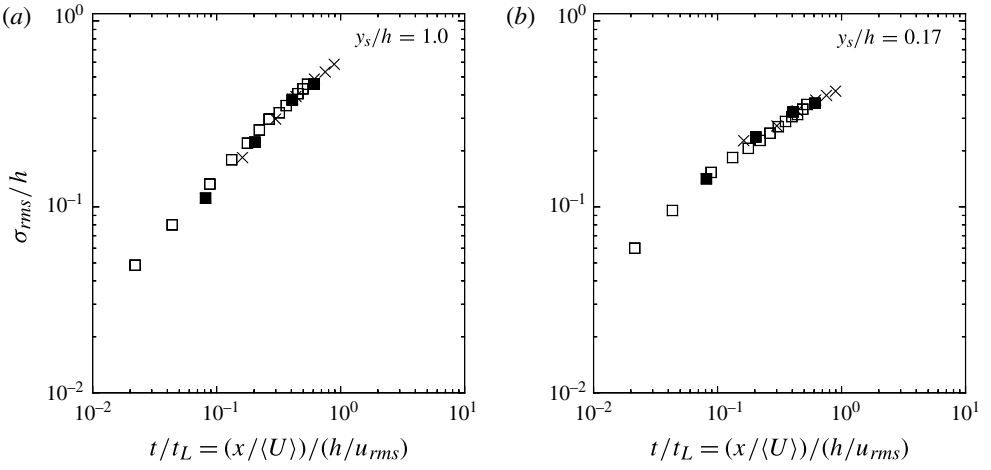

FIGURE 8. Downstream evolution of the non-dimensionalized width of the r.m.s. temperature profiles for two line source locations. Experiments (■), DNS (□) and Lavertu & Mydlarski (2005) (×).

Figures 5 and 6 respectively show the downstream decay of the peak of the mean and r.m.s. profiles normalized by a reference temperature

$$\langle \Delta T\rangle_{ref} = \frac{\displaystyle\int_0^{2h} \rho c_p \langle U\rangle \langle \Delta T\rangle \mathrm{d}y}{\displaystyle\int_0^{2h} \rho c_p \langle U\rangle \mathrm{d}y} = \frac{P_s}{\dot{m} c_p} \tag{6.2}$$

(see Incropera *et al.* 2007, p. 495), where ρ and c_p are, respectively, the density and the specific heat at constant pressure of air, $\langle U\rangle = \langle U(y)\rangle$ is the mean velocity, P_s is the power of the line source and $\dot{m}$ is the mass flow rate of air in the channel. It should be noted that the above definition of $\langle \Delta T\rangle_{ref}$ is different from that proposed by Rosset *et al.* (2001), $\langle \Delta T\rangle_{ref} = (P_s/l_s)/(\rho c_p U_s d_s)$, where P_s/l_s is the electric power per length unit injected via the line source, U_s is the mean longitudinal velocity at the source location and d_s is the source diameter. Such a reference temperature may not be appropriate if both the diameter of the source and the input power change. For instance, when d_s and P_s are each multiplied by two (assuming that the change of diameter has a negligible impact on the temperature profiles, which is reasonable for a very small diameter line source like those used herein), $\langle \Delta T\rangle_{ref}$ should also be doubled to maintain a consistent normalization, which is not the case using their definition, due to the dependence of the latter on d_s.

Figures 5 and 6 show good agreement between the numerical and experimental results, both the present ones and those of Lavertu & Mydlarski (2005). We note that the change in curvature observed in figure 5(*b*) is a consequence of the adiabatic walls. The downstream locations of the changes correspond to the locations at which the peak 'encounters' the wall, and subsequently stops spreading on that side. Due to the adiabatic boundary conditions at the wall, the peak remains at $y = 0$ for all subsequent downstream locations. A similar change in curvature was observed for plumes emanating from a near-wall source in Boppana *et al.* (2012). Such

a phenomenon, however, was absent in the case of the centreline source, as the downstream distances studied herein were not large enough for the plume to have grown sufficiently for its edges to interact with the channel walls.

The downstream evolutions of the half-widths of the mean and r.m.s. profiles (i.e. the widths of the profiles at the locations where they fall to 50 % of their peak values) are plotted in figures 7 and 8 respectively for the two source locations. The standard deviations σ are determined by best fitting a Gaussian curve to the data of figures 3 and 4. (It should be noted that the standard deviation of the Gaussian profile is linearly related to its half-width.) Once again, good agreement between experimental and numerical results is obtained. One can note that in figure 7(*b*), the standard deviation of the numerical results tends to be larger than that of the experiments for the farthest downstream distance present herein, in contrast to the results of figure 3(*b*). This difference derives from the fact that a Gaussian curve fit is not an especially accurate fit far downstream of the line source.

To complement the preceding analysis of large-scale statistics of the scalar field, we plot in figure 9 the instantaneous temperature fields generated by our DNS downstream of both a centreline and a near-wall line source. One can note the 'holes' in the temperature field for the plume emanating from the centreline source. Such holes are absent in the plume emanating from the near-wall source given the different nature of the mixing near the wall (including a reduced tendency of the plume to flap). The presence of the wall (i) limits the growth of the plume on one side, (ii) is the cause of the inhomogeneity of the flow (which is strongest near the wall) and (iii) affects the mixing, as will be further discussed.

7. Results: small-scale statistics of the scalar field

We now proceed to investigate the small-scale structure of the scalar field. Both experiments and numerical simulations are used in our analysis. We present statistics at various (downstream and transverse) locations behind the line source. The details of the measurement locations are specified in the figures.

7.1. *Spectra of* θ, ε_θ *and* $\partial\theta/\partial x_\beta$

We begin by plotting the one-dimensional longitudinal power spectra of the scalar fluctuations, $E_\theta(\kappa_1)$, where κ_1 is the longitudinal wavenumber. Results are presented for four downstream locations for each of the two line source locations studied herein, $y_s/h = 1.0$ and 0.17, in figures 10 and 11, respectively. The experimental results are obtained from time series, which provide Eulerian time spectra, $E_\theta(f)$. Eulerian spatial spectra, $E_\theta(\kappa_1)$, are obtained using Taylor's hypothesis, $E_\theta(\kappa_1) = (\langle U\rangle/(2\pi))E_\theta(f)$, where $\kappa_1 = 2\pi f/\langle U\rangle$. Taylor's hypothesis is a reasonable approximation in most regions of the flow where $u_{rms}/\langle U\rangle < 10\,\%$. (See Sreenivasan, Antonia & Danh 1977; Prasad & Sreenivasan 1990, for example.) For consistency with the experiments, the numerical spectra were also computed from time series, in order to not introduce any artificial differences associated with the (small) errors induced by the inevitable use of Taylor's hypothesis in the experiments.

To compare experiments and simulations, the abscissa and ordinates were normalized by small-scale quantities, i.e. $\varepsilon^{-3/4}\nu^{5/4}\varepsilon_{\theta_x}$ and $\eta = (\nu^3/\varepsilon)^{0.25}$. It should be noted that the dissipation rate of the turbulent kinetic energy, ε, was determined using the assumption of local isotropy, i.e. $\varepsilon = 15\nu\int_0^\infty \kappa_1^2 E_u(\kappa_1)\mathrm{d}\kappa_1$, where E_u is the power spectrum of the longitudinal velocity fluctuations. Although the complete definition of ε can be computed in the DNS, the simulations calculated η using

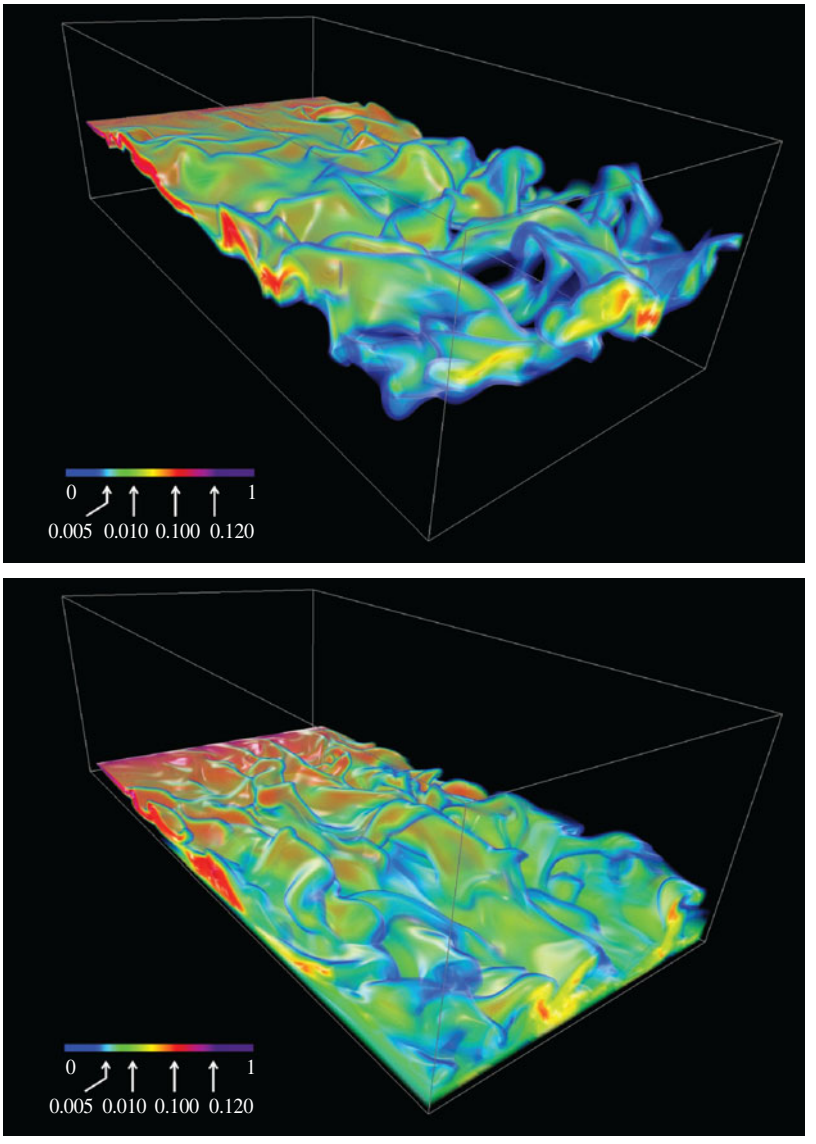

FIGURE 9. Instantaneous temperature fields generated (by DNS) downstream of line sources at two wall-normal locations, $y_s/h = 1.0$ (*a*) and $y_s/h = 0.17$ (*b*). Here, $Re_\tau = 190$ and $t^+ = 2770$ for the velocity field and $t^+ = 166$ for the scalar field (where, in the latter case, $t^+ = 0$ corresponds to the time at which the scalar is first injected into the flow). It should be noted that the scale bars are nonlinear in the non-dimensionalized temperature ($(T - T_\infty)/(T_{max} - T_\infty)$). Imagery produced by VAPOR (www.vapor.ucar.edu, see also Clyne & Rast 2005, Clyne *et al.* 2007).

the above equation so that the results would be consistent with those obtained in the experiments (for which ε can only be estimated using the assumption of local isotropy). Near the centreline, this is an excellent assumption; however, very close to the wall, at locations outside of the range of the experimental measurements undertaken in this work, it does introduce some error (Antonia, Kim & Browne

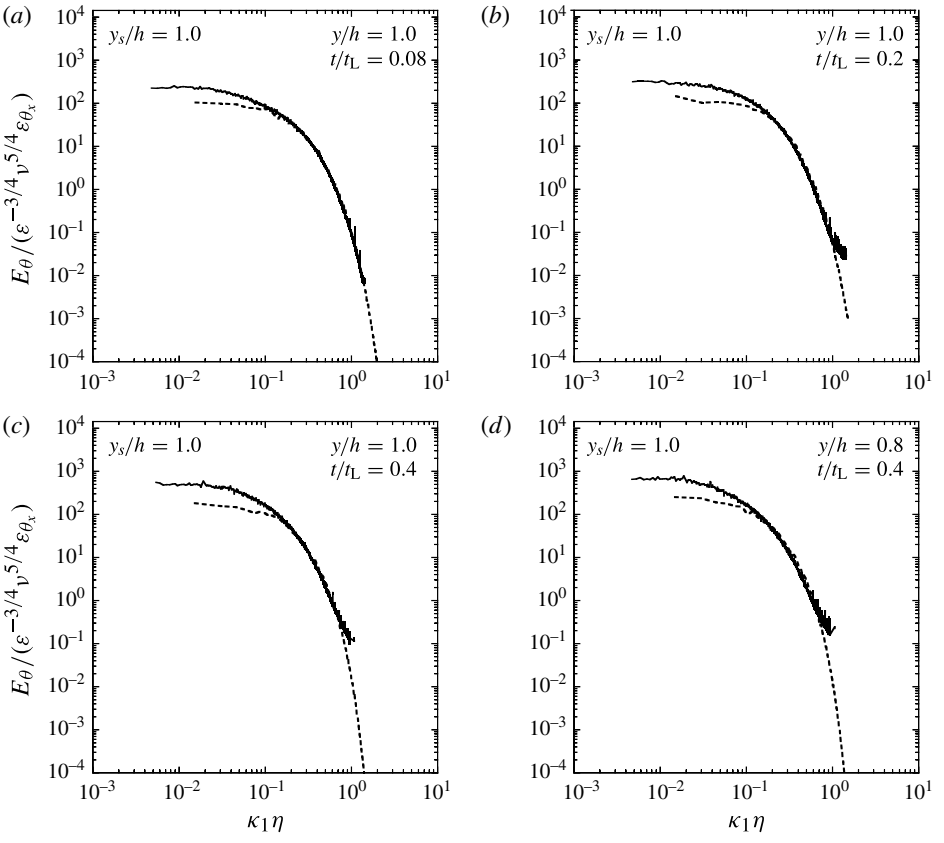

FIGURE 10. One-dimensional longitudinal spectra of the temperature fluctuations for $y_s/h = 1.0$ at three downstream locations and at two wall-normal locations. Results from experiments (solid line) and DNS (dashed line) are reported.

1991). For example, at $y/h = 0.05$ (which corresponds to $y^+ \approx 10$ in the DNS), the difference in estimates of the Kolmogorov microscale is ~2. Here, ε_{θ_x} was determined from its definition $(\alpha/\langle U\rangle^2)\langle(\partial\theta/\partial t)^2\rangle$ and also invoking Taylor's hypothesis.

Figures 10 and 11 show very good agreement between the experimental and numerical results at large κ_1, independent of the line source location. However, some differences exist at small κ_1 for the spectra measured downstream of the centreline line source (see figure 10) due to the difference in Reynolds numbers between the experimental and numerical flows. (Given that the normalization is based on small-scale quantities, one cannot expect the spectra of the two flows at different Reynolds numbers to be the same at large scales.) It should be noted that the turbulence intensity (and therefore the local Reynolds number) is higher in the near-wall region and, hence, the mixing is more effective (Lavertu & Mydlarski 2005). As a consequence, the agreement between the experimental and numerical results at small to medium κ_1 is better for the scalar field generated by the near-wall source (figure 11) than that for the centreline source (figure 10).

One-dimensional streamwise dissipation spectra, i.e. $\kappa_1^2 E_\theta(\kappa_1)$, for thermal fields originating from line sources located at $y_s/h = 1.0$ and $y_s/h = 0.17$ are plotted in figures 12 and 13, respectively. The experiments and DNS are in good agreement at

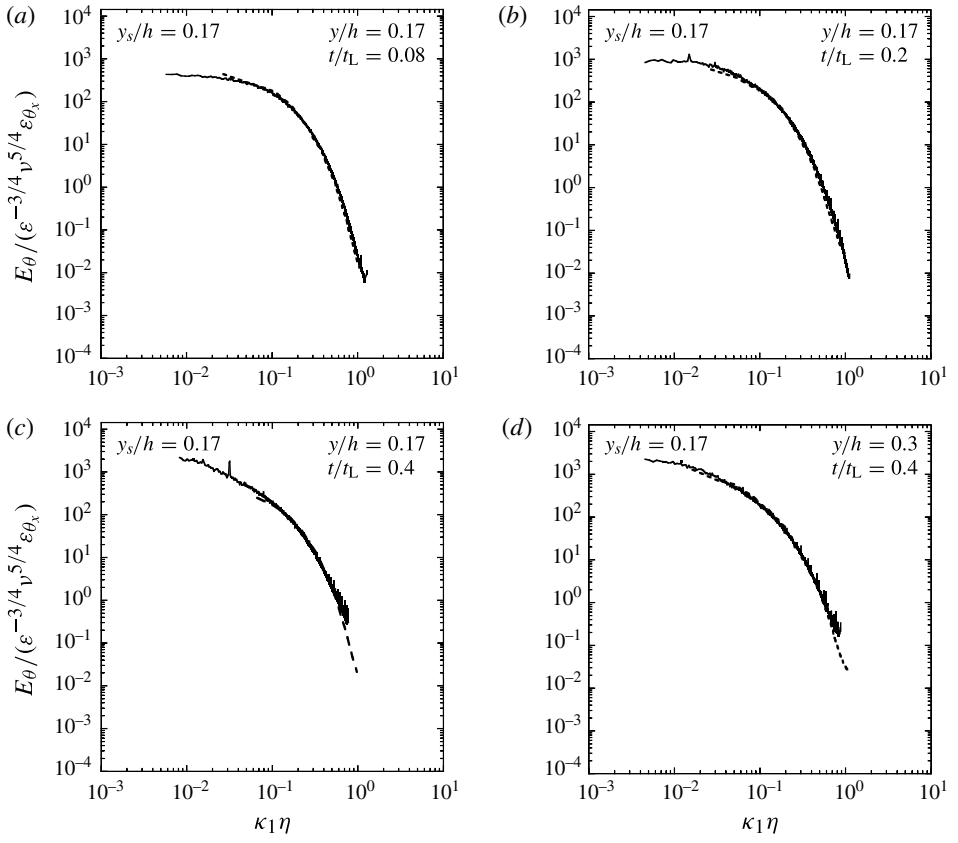

FIGURE 11. One-dimensional longitudinal spectra of the temperature fluctuations for $y_s/h = 0.17$ at three downstream locations and at two wall-normal locations. Results from experiments (solid line) and DNS (dashed line) are reported.

all measurement locations for both line source locations. It should be noted that the normalization used in these figures implies that the area under each curve is equal to the Prandtl number ($Pr = 0.7$). As previously noted, these results serve to confirm that the resolution of our DNS is sufficient to (i) accurately resolve the contributions to ε_θ and (ii) reproduce the range of length scales measured in the experiments.

The dissipation spectra are generally found to peak at $\kappa_1\eta \approx 0.2$, showing that most of the dissipation occurs at length scales five times larger than η, consistent with the findings of Kozuka *et al.* (2009). However, a slight drift of the peak locations with increasing downstream distance from larger to smaller κ_1 for the centreline source is observed. (The peak occurs at $\kappa_1\eta = 0.26$, 0.21 and 0.17 for $t/t_L = 0.08$, 0.2 and 0.4, respectively.) Such a trend is not observed downstream of the near-wall sources. This may be attributed to the increased mixing that occurs near the wall (Lavertu & Mydlarski 2005).

We now proceed to analyse the components of the dissipation spectra by examining the one-dimensional spectra of the temperature derivative $\partial\theta/\partial\beta$, where $\partial\theta/\partial\beta$ is the β-derivative of the scalar fluctuations ($\beta = x$, y or z). To this end, figures 14 and 15 plot spectra of the streamwise (x), wall-normal (y) and spanwise (z) components of the fluctuating temperature gradient, i.e. $E_{\partial\theta/\partial\beta}$. Here, $E_{\partial\theta/\partial x}$ was measured by

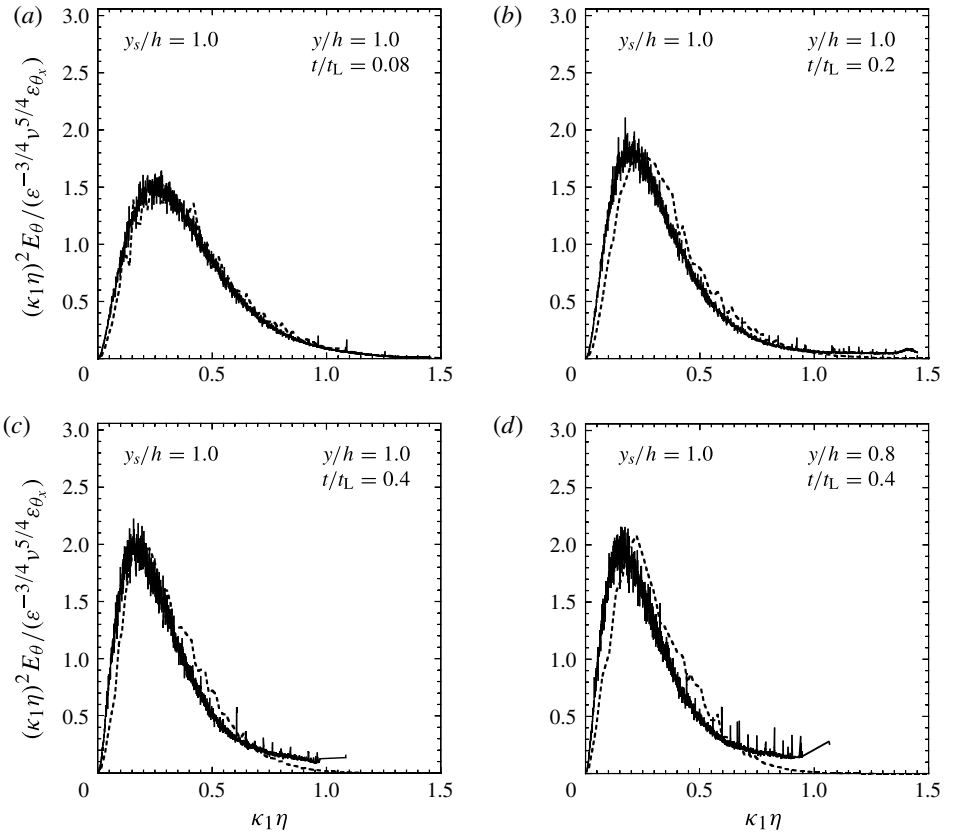

FIGURE 12. One-dimensional longitudinal dissipation spectra of the temperature fluctuations for $y_s/h = 1.0$ at three downstream locations and at two wall-normal locations. Results from experiments (solid line) and DNS (dashed line) are reported.

assuming Taylor's hypothesis, whereas the other two components were measured using a second-order finite difference approximation. It should be noted that the streamwise (one-dimensional) spectrum tends towards zero at large scales, which differs from the two other spectra which are subject to aliasing and have finite values at zero wavenumber (Van Atta 1991). This difference is therefore not dynamical and thus is not indicative of a lack of local isotropy. It should be noted that the spectra were normalized by $\varepsilon_\theta\eta/\nu$, where $\varepsilon_\theta = \varepsilon_{\theta_x} + \varepsilon_{\theta_y} + \varepsilon_{\theta_z}$ and where η was computed using the assumption of local isotropy.

The present spectra are similar to those reported by Van Atta (1991) and Thoroddsen & Van Atta (1996), who studied scalar dissipation in decaying stably stratified grid turbulence. The authors showed that the large and small scales are anisotropic near the grid but become strongly anisotropic farther downstream in their stratified flow. Interestingly, they noticed that all scales develop anisotropies at about the same rate.

In the present research, the scalar is injected in a highly anisotropic manner that produces sharp gradients in the y direction in the vicinity of the source. This anisotropy is shown in both figures 14(*a*) and 15(*a*), where $\varepsilon_{\theta_y} > \varepsilon_{\theta_z}$. However, the gap between ε_{θ_y} and ε_{θ_z} diminishes considerably with increasing downstream distance.

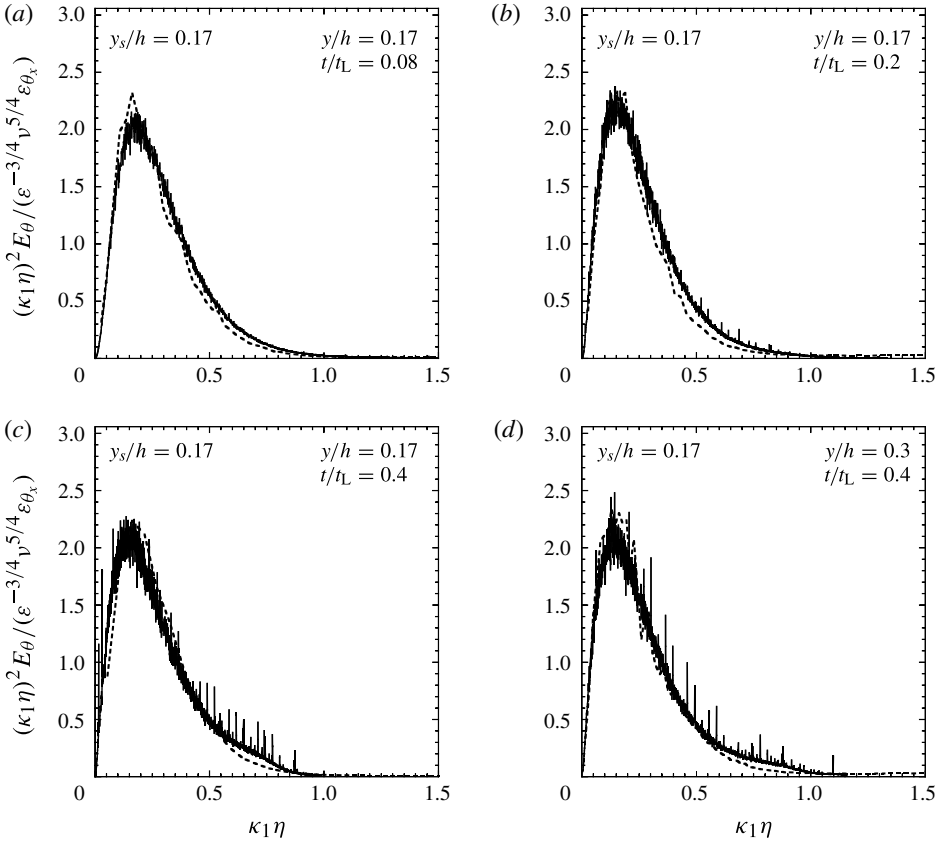

FIGURE 13. One-dimensional longitudinal dissipation spectra of the temperature fluctuations for $y_s/h = 0.17$ at three downstream locations and at two wall-normal locations. Results from experiments (solid line) and DNS (dashed line) are reported.

Ultimately, the experimentally measured spectra of ε_{θ_y} and ε_{θ_z} at $t/t_L = 0.4$ (figure 14*c*) are almost indistinguishable, which shows a clear tendency of the scalar dissipation rate towards isotropy. It is also interesting to note that the collapse between the spectra of ε_{θ_y} and ε_{θ_z} appears even sooner when the source is in the near-wall region (i.e. $t/t_L = 0.2$ as shown in 15*b*). This can again be attributed to the higher turbulence intensity (and therefore better mixing) that occurs in the near-wall region.

Figures 14 and 15 exhibit good agreement between the experiments and DNS at large wavenumbers, especially for the centreline line source. Furthermore, a similar good agreement is also reported at small wavenumbers when the line source is located at the centreline, which reinforces the validity of the results presented herein. However, discrepancies exist at small wavenumbers when the line source is in the near-wall region. The numerical results exhibit a persistent anisotropy between ε_{θ_y} and ε_{θ_z} when $y_s/h = 0.17$. These discrepancies are related to the production of ε_θ by mean velocity gradients, which occurs away from the centreline, near the wall. This effect will be discussed in more detail further on in this section. The reader is also referred to Gonzalez (2000), in which the effects of mean velocity and temperature gradients on the isotropy of ε_θ are described in detail.

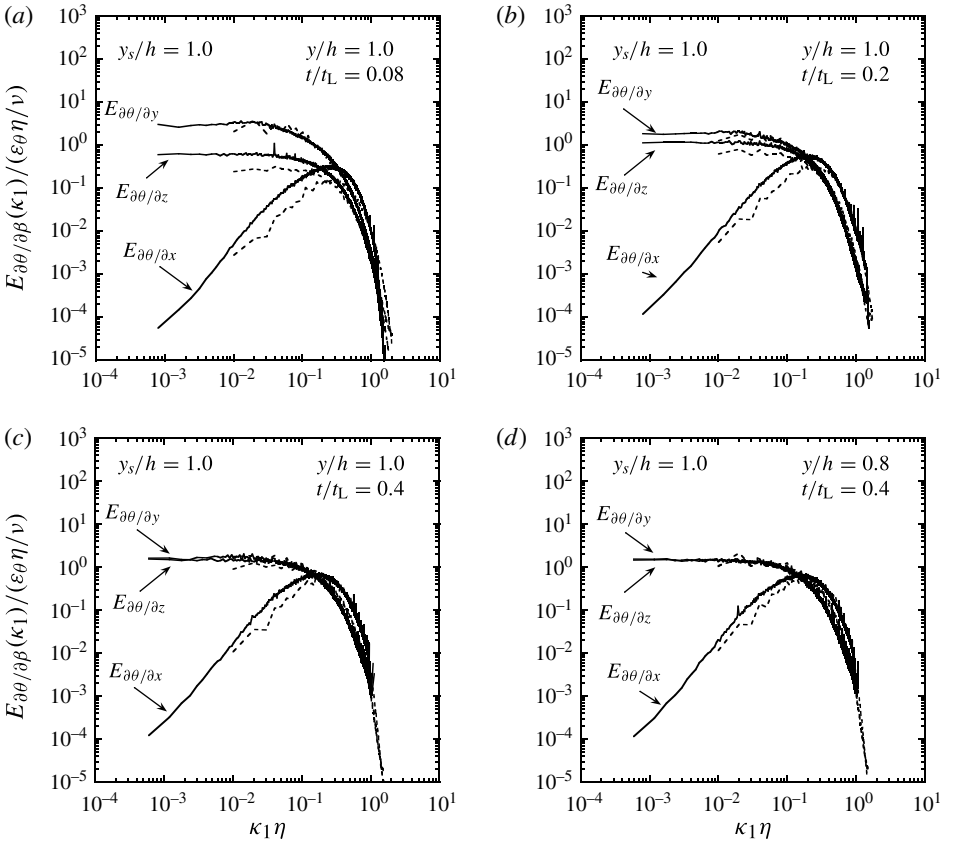

FIGURE 14. One-dimensional spectra of the temperature derivatives ($\partial\theta/\partial\beta$, where $\beta = x, y$ or z) for $y_s/h = 1.0$ at three downstream locations and at two wall-normal locations. Results from experiments (solid line) and DNS (dashed line) are reported.

7.2. *The p.d.f.s of* $\partial\theta/\partial x_\beta$ *and* ε_θ

The p.d.f.s of the temperature derivatives are plotted in figures 16 and 17 for line sources located at $y_s/h = 1.0$ and 0.17, respectively. The p.d.f.s of the three components are quite different from each other near the source and become similar at the farthest downstream distance, where they develop quasi-exponential tails. Close to the source, figure 16(*a*) shows three peaks in the simulated p.d.f. of the wall-normal temperature derivative, $P(\partial\theta/\partial y)$, whereas the p.d.f.s of the other two derivatives are unimodal. These triple peaks are due to the nature of the temperature field immediately downstream of the source. For very small t/t_L, the plume has a top-hat profile and thus we expect the p.d.f. to be given by two delta functions where the two peaks are nominally at $\pm\,(T_{wire} - T_\infty)\,/(d_s/2)$, where d_s is the source diameter. However, slightly farther away from the source, after some mixing has occurred, the principal peak (or mode) starts to emerge while the other two initial peaks recede. Even further away from the source, the peaks from the initial top-hat profile disappear and the p.d.f. develops exponential tails, in this case characteristic of a well-mixed scalar. In the near-wall region, as the mixing is better, the initial peaks disappear very quickly and the initial trimodal p.d.f. is not observed for the measurement locations considered herein. For a similar reason, the experimentally measured $P(\partial\theta/\partial y)$ (as it

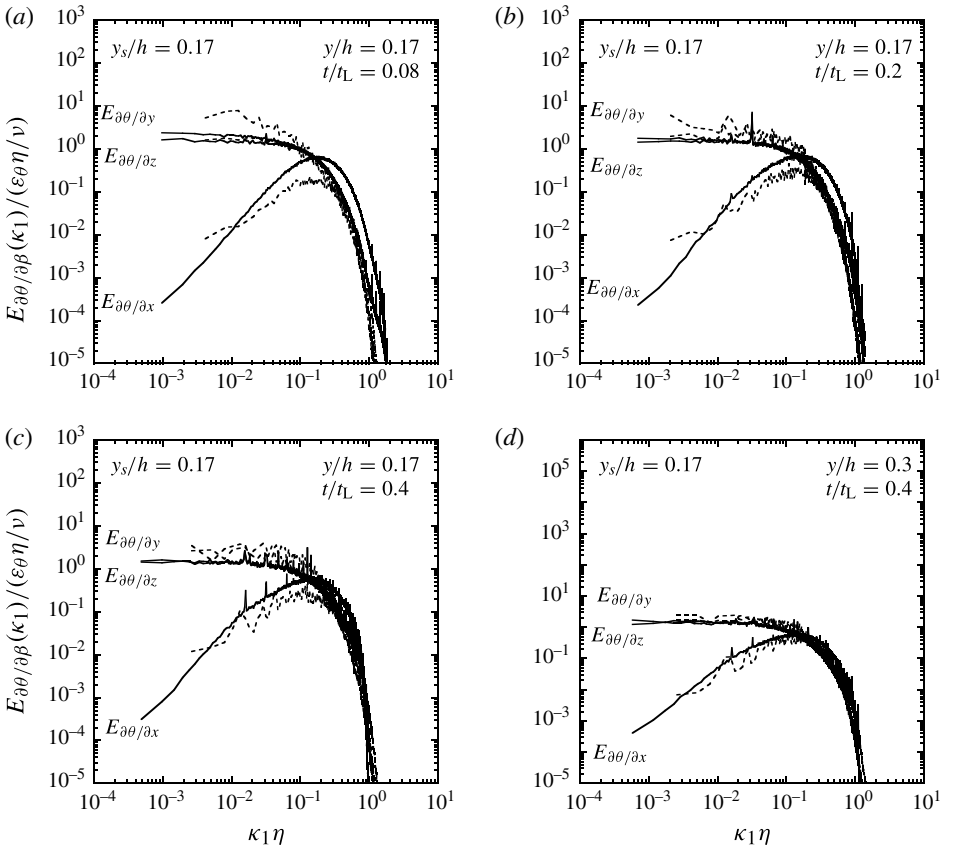

FIGURE 15. One-dimensional spectra of the temperature derivatives ($\partial\theta/\partial\beta$, where $\beta = x, y$ or z) for $y_s/h = 0.17$ at three downstream locations and at two wall-normal locations. Results from experiments (solid line) and DNS (dashed line) are reported.

is at a higher Reynolds number) is also unimodal, although of a shape that would be consistent with a trimodal p.d.f. farther upstream. In addition, it is worth noting that the quasi-exponential tails appear sooner for the near-wall line source than when the line source is at the centreline.

To further study the evolution of the small-scale scalar field, figure 18 examines the p.d.f.s of ε_θ for the centreline source in figure 18(*a*), and those of the near-wall source in figure 18(*b*). We remark that we plot the p.d.f. of the natural logarithm of ε_θ, $\ln(\varepsilon_\theta)$, to verify whether the p.d.f.s of ε_θ exhibit a log-normal distribution, as has been hypothesized (e.g. Gurvich & Yaglom 1967) and observed in situations where the scalar is injected at large scales (e.g. Sreenivasan *et al.* 1977, Dahm & Buch 1989, Su & Clemens 2003, Schumacher & Sreenivasan 2005, Sutton & Driscoll 2013), albeit with small departures, which may or may not be significant (Holzer & Siggia 1994). Plotting of the p.d.f.s in log-linear coordinates (i) renders log-normal distributions to appear as concave-down parabolas and (ii) emphasizes the tails of the p.d.f.s. In the most extreme case (closest to the source for $y_s/h = 1.0$), the p.d.f. of ε_θ is clearly not log-normal, having a distinct peak and tails for small values of ε_θ (i.e. their left tails), which verge on exponential behaviour. As previously observed (e.g. Lavertu & Mydlarski 2005), the centreline plume flaps more because (i) it is not bounded

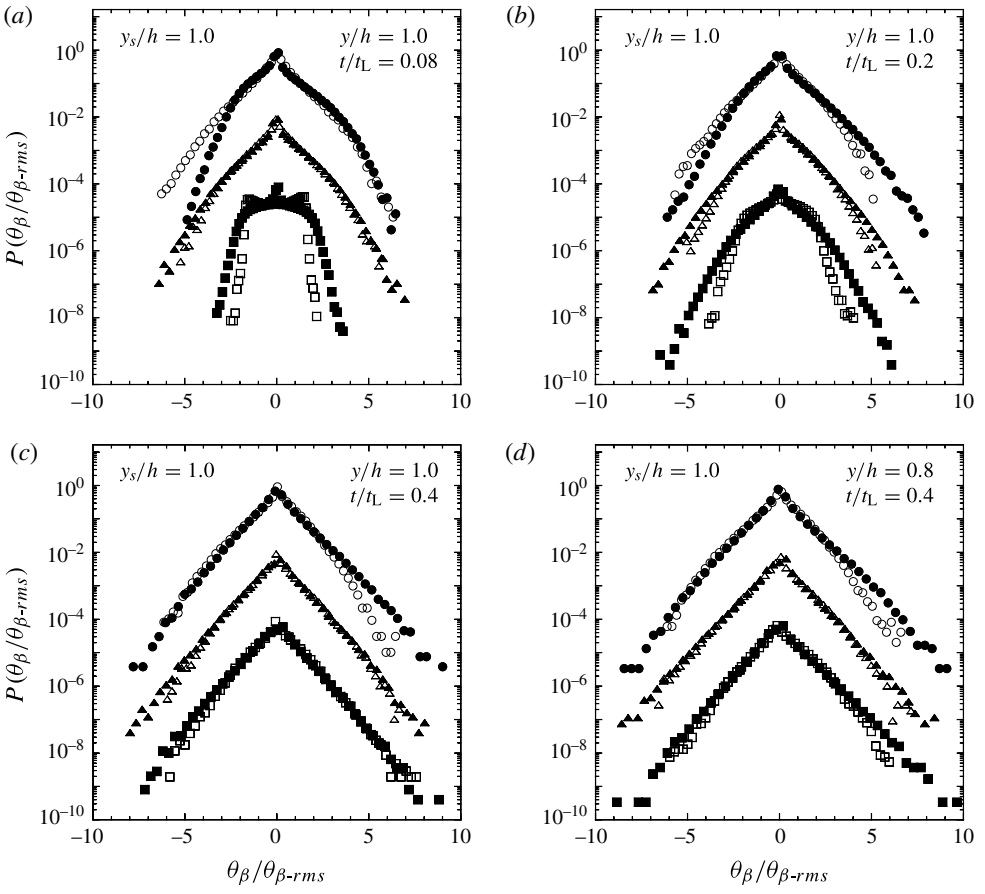

FIGURE 16. The p.d.f.s of the temperature derivatives ($\partial\theta/\partial\beta$, where $\beta = x, y$ or z) for $y_s/h = 1.0$ at three downstream locations and at two wall-normal locations. Experimental and DNS results are respectively denoted by the filled symbols ($\partial\theta/\partial x$ (●), $\partial\theta/\partial y$ (■) and $\partial\theta/\partial z$ (▲)) and the empty symbols ($\partial\theta/\partial x$ (○), $\partial\theta/\partial y$ (□) and $\partial\theta/\partial z$ (△)). The curve for $P((\partial\theta/\partial x)/(\partial\theta/\partial x)_{rms})$ is plotted normally, whereas the remaining curves are offset downwards in increments of two decades.

on one side (by the wall) and (ii) the intensity of the turbulence (and therefore the mixing) is lower at the centreline than it is near the wall, where u_{rms} increases due to increased production of turbulent kinetic energy. Consequently, the possibility of measuring small values of ε_θ for the plume generated by the centreline source is increased due to (i) smaller measured temperature differences due to the increased bulk motion of the plume and (ii) increased measurements made outside of the plume. As t/t_L (or equivalently x/h) increases, and as the wall is approached, the p.d.f.s of ε_θ evolve, becoming more log-normal in nature, presumably due to the reduced flapping of the plume (as it widens with increasing t/t_L) and the more intense turbulent mixing that occurs near the wall. Such variations in the shape of the p.d.f. of ε_θ need to be accounted for to accurately model the scalar mixing process, such as the one occurring in a combustion chamber where the fuel is injected at small scales. The assumption of a constant shape (e.g. log-normal) of the p.d.f. of ε_θ would clearly be inaccurate

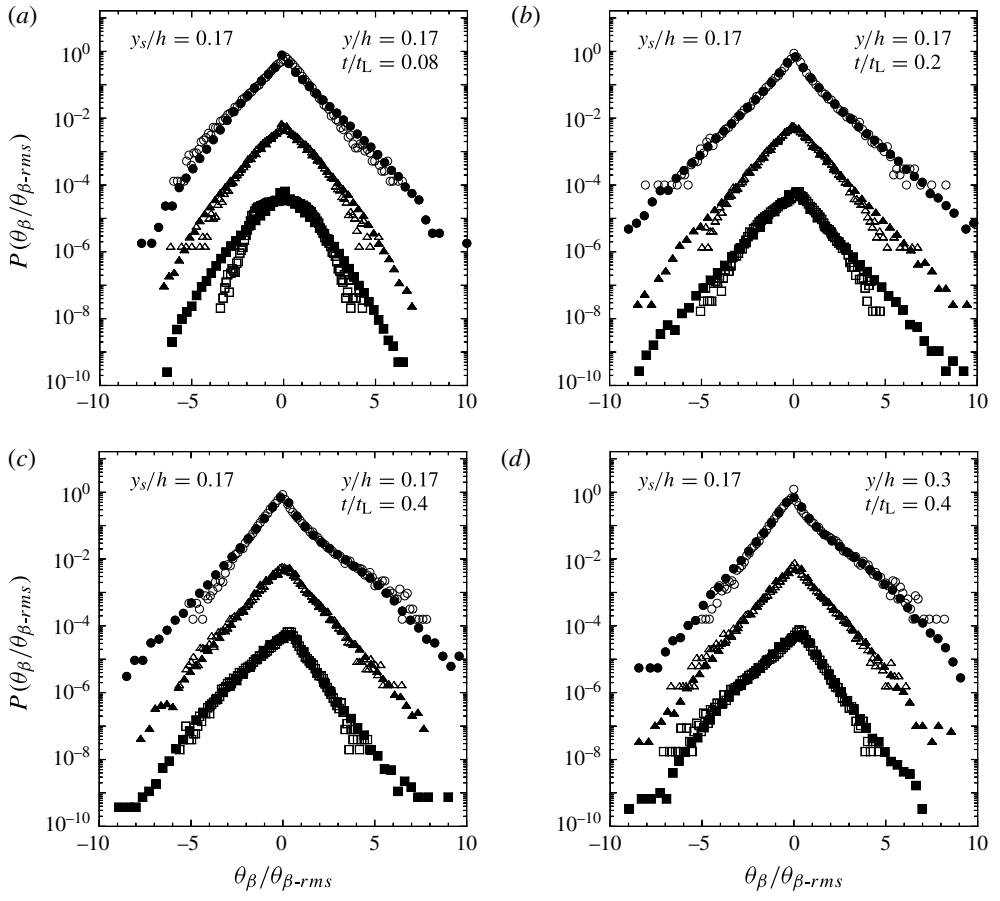

FIGURE 17. The p.d.f.s of the temperature derivatives ($\theta_\beta \equiv \partial\theta/\partial\beta$, where $\beta = x$, y or z) for $y_s/h = 0.17$ at three downstream locations and at two wall-normal locations. Experimental and DNS results are respectively denoted by the filled symbols ($\partial\theta/\partial x$ (●), $\partial\theta/\partial y$ (■) and $\partial\theta/\partial z$ (▲)) and the empty symbols ($\partial\theta/\partial x$ (○), $\partial\theta/\partial y$ (□) and $\partial\theta/\partial z$ (△)). The curve for $P((\partial\theta/\partial x)/(\partial\theta/\partial x)_{rms})$ is plotted normally, whereas the remaining curves are offset downwards in increments of two decades.

over significant regions of the flow in situations where a scalar is injected at small scales.

7.3. *The evolution of* ε_θ

The instantaneous fields of the (total and three components of the) scalar dissipation rate (i.e. ε_θ, ε_{θ_x}, ε_{θ_y} and ε_{θ_z}) are plotted in figure 19. These are presented to provide qualitative insight into the scalar dissipation rate. In the analysis that follows, we quantitatively discuss the evolution of ε_θ and its components by analyzing specific statistics related to these quantities. For example, it is already evident from figure 19 that the largest contribution to ε_θ comes from ε_{θ_y}. However, one can also observe that its relative contribution to ε_θ decreases with increasing downstream distance, as will be elaborated upon below. We encourage the reader to refer back to these plots for further insight in the course of the subsequent discussion.

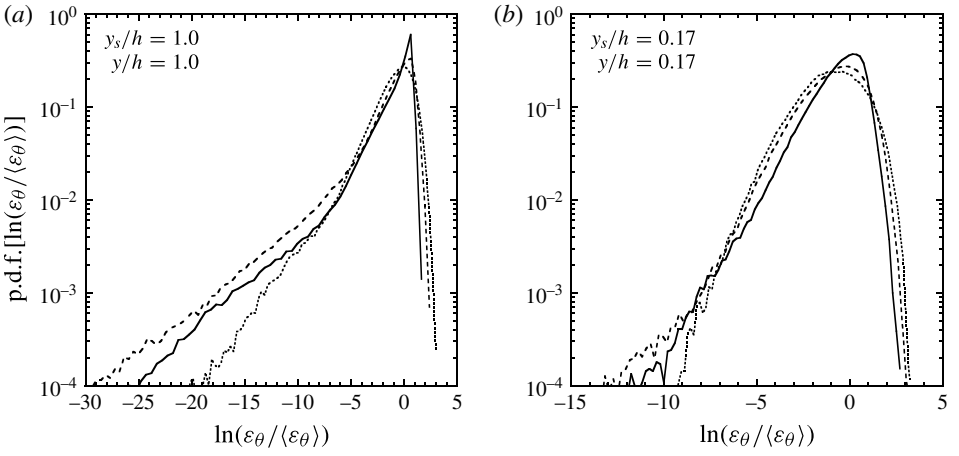

FIGURE 18. The p.d.f.s of (the natural logarithm of) $\varepsilon_\theta/\langle\varepsilon_\theta\rangle$ for two source locations and for three downstream locations, $t/t_L = 0.08$ (——), $t/t_L = 0.2$ (- - - -) and $t/t_L = 0.4$ (·····). Only DNS results are presented given that the three components of ε_θ are not measured simultaneously.

Wall-normal profiles of the three components of the scalar dissipation rate are reported in figure 20 for two downstream locations and two source locations, where the scalar dissipation rate has been scaled by $t_L/\langle\Delta T\rangle^2_{ref}$.

For $y_s/h = 1.0$, figure 20 shows that the three components of the scalar dissipation rate have approximately Gaussian profiles with maxima at the channel centreline. Outside the plume, a plateau is observed in the experimental data due to the non-zero ambient noise (i.e. noise measured by the cold-wire thermometer outside the thermal plume, which includes (i) electronic noise, (ii) actual temperature fluctuations in the free-stream flow, which is never perfectly isothermal, and (iii) a negligible contamination by the velocity fluctuations being erroneously recorded as temperature fluctuations). Small-scale anisotropy is observed near the source ($t/t_L = 0.08$), where $\varepsilon_{\theta_y} > \varepsilon_{\theta_z} \approx \varepsilon_{\theta_x}$. Farther downstream ($t/t_L = 0.4$), the gap between the three components of ε_θ is considerably reduced.

For $y_s/h = 0.17$, figure 20 shows, first, that the experimental data appear to be more isotropic, presumably due to their larger Reynolds number, whereas the DNS data exhibit differences between the three components ($\varepsilon_{\theta_y} > \varepsilon_{\theta_z} > \varepsilon_{\theta_x}$). Furthermore, the peak of ε_{θ_y} (the largest component) measured from the DNS remains downstream of the source location for all measurement locations presented herein, whereas the peak of ε_{θ_y} measured in the experiments drifts towards the channel centreline. This may be explained by the prominence in the DNS of the mechanism of production of ε_{θ_y} due to mean velocity gradients (which, as previously mentioned, will be discussed shortly). The movement in the peak of the scalar dissipation profile recalls the drift observed in the r.m.s. profiles. It should be noted that in both the experiments and the DNS, the peaks of the ε_{θ_x} and ε_{θ_z} profiles drift towards the centreline as t/t_L is increased (but the rate at which they do so is faster for the experiments). ε_{θ_y} also remains the largest component. It should also be noted that if the scalar were injected uniformly, one might expect that the scalar dissipation would peak near the region of maximum shear. (It should be recalled that in a turbulent channel flow, the turbulence intensity is maximum in the buffer layer, i.e. $y^+ \in [5, 30]$. In the present

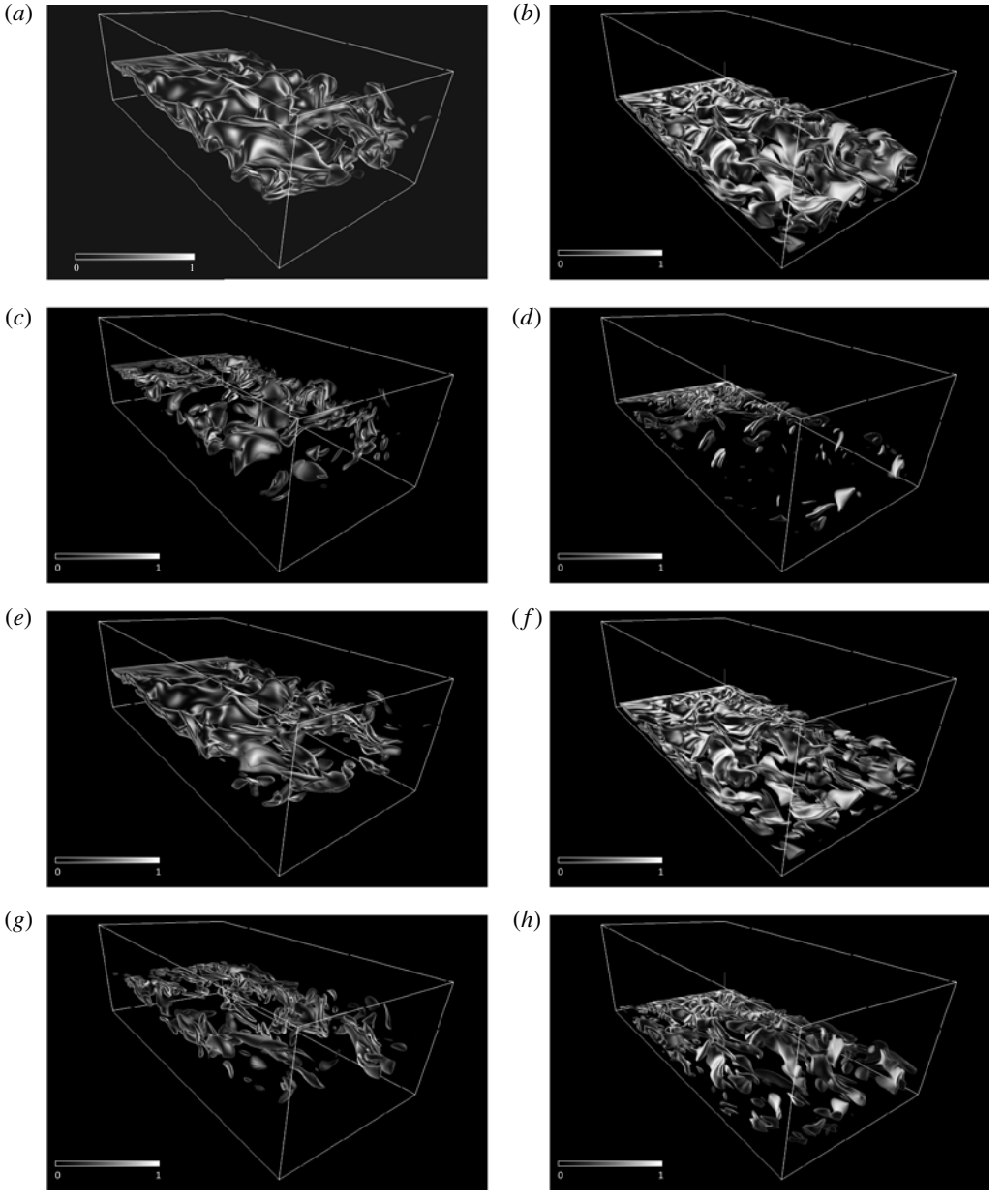

FIGURE 19. Instantaneous scalar dissipation rate fields, total and individual components, generated (by DNS) downstream of a line source at two wall-normal locations, $y_s/h = 1.0$ (*a*), (*c*), (*e*) and (*g*), $y_s/h = 0.17$ (*b*), (*d*), (*f*) and (*h*). Here, $\alpha(\partial\theta/\partial x_i)^2$ is given in (*a*) and (*b*), $\alpha(\partial\theta/\partial x)^2$ is given in (*c*) and (*d*), $\alpha(\partial\theta/\partial y)^2$ is given in (*e*) and (*f*), and $\alpha(\partial\theta/\partial z)^2$ is given in (*g*) and (*h*); $Re_\tau = 190$; $t^+ = 2770$ for the velocity field and $t^+ = 166$ for the scalar field (where, in the latter case, $t^+ = 0$ corresponds to the time at which the scalar is first injected into the flow). It should be noted that the scale bars correspond to the instantaneous scalar dissipation rates non-dimensionalized by $\varepsilon_\theta(t/t_L = 0.08, y/h = 1.0; y_s/h = 1.0)$. Imagery produced by VAPOR (www.vapor.ucar.edu; see also Clyne & Rast 2005, Clyne *et al.* 2007).

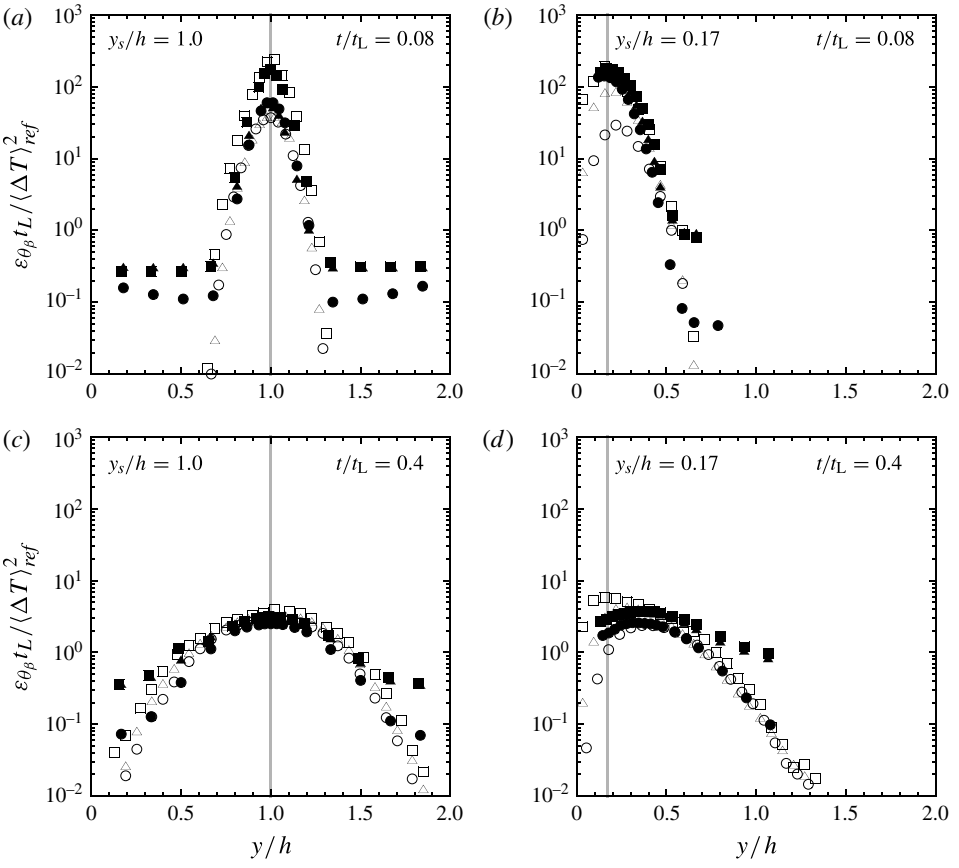

FIGURE 20. Wall-normal evolutions of the three components of the scalar dissipation rate. The experimental results are denoted by the filled symbols (ε_{θ_x} (●), ε_{θ_y} (■) and ε_{θ_z} (▲)) and the numerical results are denoted by the empty symbols (ε_{θ_x} (○), ε_{θ_y} (□) and ε_{θ_z} (△)). The vertical line indicates the transverse location of the source.

flows, $y^+ = 15$ corresponds to $y/h = 0.03$ and $y/h = 0.08$ in the experiments and the DNS, respectively.)

The evolution of the peak of the dissipation profile is somewhat similar to the evolution of the peak of the r.m.s. profile (see figure 4*b*). Previous researchers have attempted to establish a parallel between the location of the maximum of the dissipation and that of the maximum temperature fluctuations. For instance, Lockwood & Moneib (1980) measured the fluctuating temperature in a heated round turbulent free jet. They showed that the scalar dissipation rate of a turbulent jet attains its maximum at the location of the maximum of the temperature fluctuation intensity. However, this conclusion was contradicted by the observations of Antonia & Mi (1993), who studied the temperature 'jumps' (relatively sudden increases in temperature followed by gradual decreases, also known as 'ramp–cliff' structures) in a heated turbulent jet and attempted to estimate their contributions to the temperature dissipation. They showed that although the temperature 'jumps' contributed to an increase in the temperature variance, their contribution to the scalar dissipation rate was small.

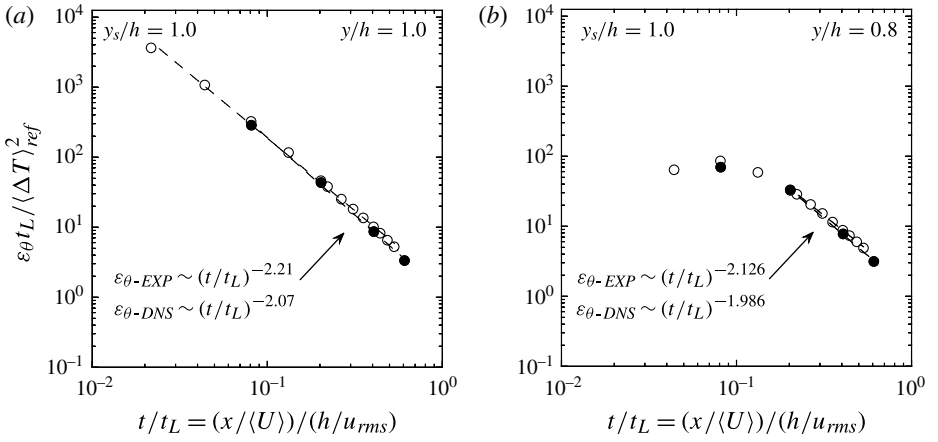

FIGURE 21. The downstream evolution of the total scalar dissipation rate for $y_s/h = 1.0$ at two wall-normal locations. The experimental results are denoted by the filled symbols and the numerical results are denoted by the empty symbols. The solid and dashed lines are the best-fit power laws to the experimental and numerical data, respectively.

The downstream evolution of the centreline ($y/h = 1.0$) and the off-centreline ($y/h = 0.8$) mean thermal dissipation is shown in figure 21 for $y_s/h = 1.0$. At the centreline, the experiments and DNS both exhibit a power-law decay of the form $\varepsilon_\theta \sim (t/t_L)^n$, where n varies between -2.2 and -2.0, with the experiments tending to exhibit slightly more negative decay exponents. Away from the centreline, a power-law decay is also observed, but only after a certain distance downstream ($t/t_L \gtrsim 0.2$), which approximately corresponds to the point at which the plume is wide enough so that the sensor (located at $y/h = 0.8$) no longer measures outside of the plume as it flaps. Analogous plots for the near-wall source are also given in figure 22. As for $y_s/h = 1.0$, the dissipation is maximum in the vicinity of the source and exhibits a power-law decay with similar values of the decay exponents, with the experiments again tending to exhibit a slightly more rapid decay. Given the larger values of ε_θ measured in the central region of the plume, one can furthermore conclude that the efficiency in smearing the fluctuations in the scalar field is larger behind the source than at the edges of the plume. However, at the farthest downstream location, the difference between the two is smaller than 8 %, indicating that ε_θ tends to become more uniform inside the plume as it expands, as observed in figure 20. We also note that Rosset *et al.* (2001) found $\varepsilon_\theta \sim x^{-2.5}$ downstream of a heated line source placed in a turbulent boundary layer. Their decay exponent, albeit slightly more negative, is quite similar to the values measured herein, despite the differences in flow geometry, Reynolds number, line source location, etc.

To investigate the evolution of the components of the scalar dissipation rate and their anisotropy, figures 23 and 24 plot the evolution of $\varepsilon_{\theta_\beta}/\varepsilon_{\theta_\gamma}$, where the indices β and γ can be x, y or z, and where $\beta \neq \gamma$. For a locally isotropic scalar field, this ratio must be equal to 1. When the line source is at the centreline, both the experiments and the DNS show that the anisotropy is reduced and the components of the scalar dissipation rates converge towards an isotropic state. Near the source, however, the dissipation is predominantly in the y direction due to the sharp temperature gradients ($\partial\theta/\partial y$) there that are associated with the plume boundary. The dissipations in the other two directions ($\partial\theta/\partial x$ and $\partial\theta/\partial z$) are almost equal, indicative of the

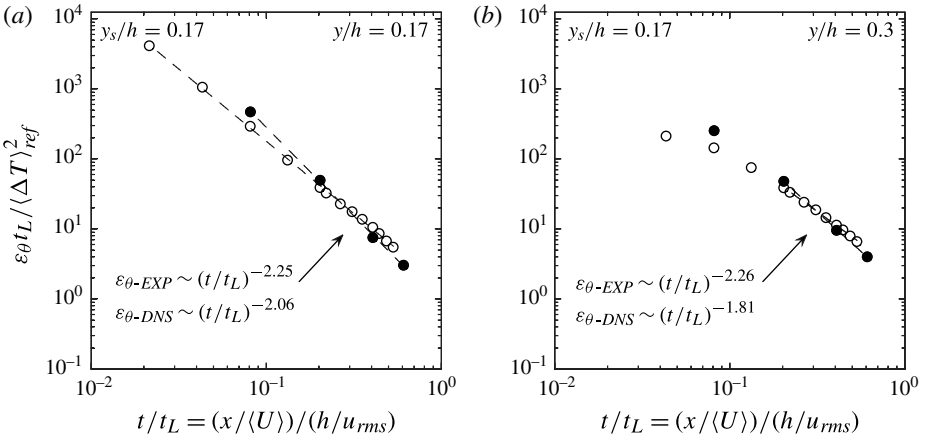

FIGURE 22. The downstream evolution of the total scalar dissipation rate for $y_s/h = 0.17$ at two wall-normal locations. The experimental results are denoted by the filled symbols and the numerical results are denoted by the empty symbols. The solid and dashed lines are the best-fit power laws to the experimental and numerical data, respectively.

quasi-axisymmetric nature of the turbulence at that location. For the near-wall source, figure 24 indicates that (i) the agreement between the experiments and the DNS is not as good as it is for the centreline source, with the experiments being notably more isotropic than the DNS. Furthermore, it is noted that the anisotropy is stronger when measured at $y/h = 0.17$ than at $y/h = 0.3$, indicating that there exist regions in the channel flow field that better lend themselves to returning to an isotropic state. We will subsequently argue that the anisotropy is dependent on the presence of velocity gradients (Antonia & Browne 1986; Gonzalez 2000), as well as the Reynolds number of the flow. In this vein, we remark that the anisotropy measured in the experiments is less strong than in the DNS, presumably due to its larger Reynolds numbers, which (i) results from a more rapid elimination of the large-scale anisotropy associated with the injection of the scalar and (ii) explains the discrepancies observed in figure 24. Moreover, it can be noted that the flow is no longer (quasi-)homogeneous in the regions plotted in figure 24, so the equal offset of the anisotropy of ε_{θ_y} by ε_{θ_x} and ε_{θ_z} is not observed here (like in figure 23). Regarding these figures, we finally note that the measured increase in anisotropy observed in figures 23(*b*) and 24 is presumably due to experimental errors arising from the low signal-to-noise ratio at the farthest downstream location ($t/t_L = 0.6$).

The small-scale anisotropy of the scalar field can also be examined using third-order statistics, most notably the skewness of the scalar derivative, which must be zero in a locally isotropic flow. Figure 25 plots the transverse profiles of the skewness of $(\partial\theta/\partial\beta)$, $S_{\partial\theta/\partial\beta} \equiv \langle(\partial\theta/\partial\beta)^3\rangle/\langle(\partial\theta/\partial\beta)^2\rangle^{3/2}$, where β is equal to x, y or z. When $y_s/h = 1.0$, we observe that $S_{\partial\theta/\partial x}$ and $S_{\partial\theta/\partial z}$ are close to zero in the inner core of the plume, where the former is consistent with local isotropy, but the latter is simply symptomatic of the homogeneity of the flow in the z direction. Here, $S_{\partial\theta/\partial y}$ is an odd function of y/h due to the underlying symmetries of the flow when $y_s/h = 1.0$, and changes sign depending on which side of the flapping plume the sensor is located. Thus, its zero value at $y/h = 1.0$ does not result from local isotropy at that location, but is rather a consequence of the underlying symmetries in this case. When $y_s/h = 0.17$, persistent anisotropy in $S_{\partial\theta/\partial x}$ and $S_{\partial\theta/\partial y}$ is observed, although it is (i) lesser

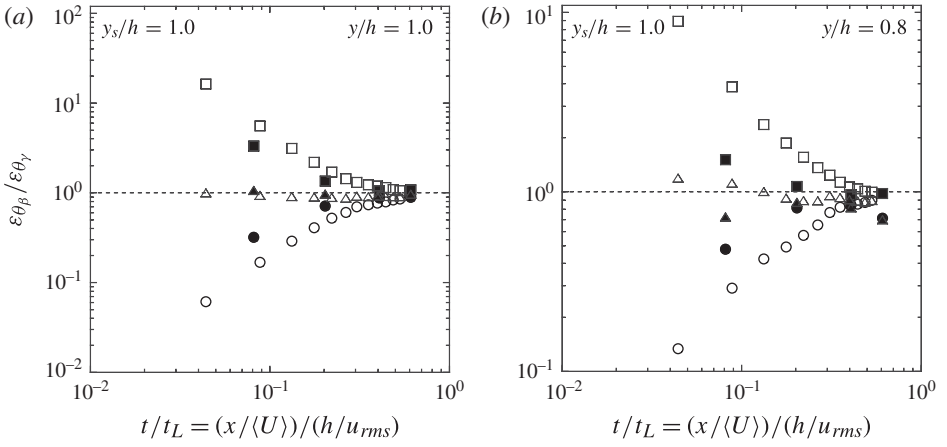

FIGURE 23. The downstream evolution of the ratios $\varepsilon_{\theta_\beta}/\varepsilon_{\theta_\gamma}$ (where β and $\gamma = x$, y or z and $\beta \neq \gamma$) for $y_s/h = 1.0$ at two wall-normal locations. The experimental results are denoted by the filled symbols ($\varepsilon_{\theta_x}/\varepsilon_{\theta_y}$ (●), $\varepsilon_{\theta_y}/\varepsilon_{\theta_z}$ (■) and $\varepsilon_{\theta_x}/\varepsilon_{\theta_z}$ (▲)) and the numerical results are denoted by the empty symbols ($\varepsilon_{\theta_x}/\varepsilon_{\theta_y}$ (○), $\varepsilon_{\theta_y}/\varepsilon_{\theta_z}$ (□) and $\varepsilon_{\theta_x}/\varepsilon_{\theta_z}$ (△)).

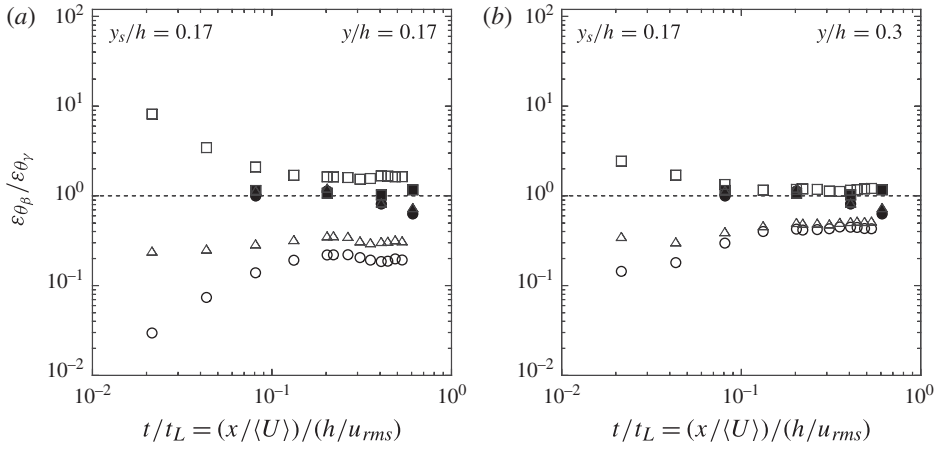

FIGURE 24. The downstream evolution of the ratios $\varepsilon_{\theta_\beta}/\varepsilon_{\theta_\gamma}$ (where β and $\gamma = x$, y or z and $\beta \neq \gamma$) for $y_s/h = 0.17$ at two wall-normal locations. The experimental results are denoted by the filled symbols ($\varepsilon_{\theta_x}/\varepsilon_{\theta_y}$ (●), $\varepsilon_{\theta_y}/\varepsilon_{\theta_z}$ (■) and $\varepsilon_{\theta_x}/\varepsilon_{\theta_z}$ (▲)) and the numerical results are denoted by the empty symbols ($\varepsilon_{\theta_x}/\varepsilon_{\theta_y}$ (○), $\varepsilon_{\theta_y}/\varepsilon_{\theta_z}$ (□) and $\varepsilon_{\theta_x}/\varepsilon_{\theta_z}$ (△)).

in magnitude for the experimental data and (ii) more uniform over the extent of the plume. However, $S_{\partial\theta/\partial z}$ is zero in both cases once again, as expected.

From figures 23 and 24, one observes that the end of the period of isotropization occurs within a few tenths of $t_L(\equiv h/u_{rms})$. It is therefore of interest to see how this time scale relates to the mechanical or thermal time scales of the flow. To this end, figure 26 plots the transverse profiles of both the (experimental and numerical) mechanical and thermal time scales normalized by t_L, $(k/\varepsilon)/t_L$ and $(\langle\theta^2\rangle/\varepsilon_\theta)/t_L$, respectively. The latter are plotted at three downstream locations ($t/t_L = 0.08$, 0.2 and 0.4), whereas the former is the same for all downstream distances in this fully

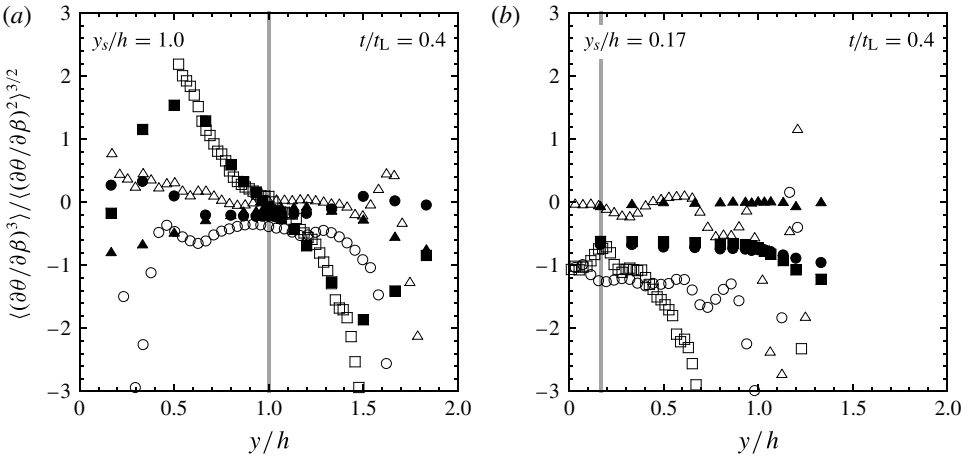

FIGURE 25. Transverse profiles of the skewness of the scalar derivative, $S_{\partial\theta/\partial\beta} \equiv \langle(\partial\theta/\partial\beta)^3\rangle/\langle(\partial\theta/\partial\beta)^2\rangle^{3/2}$, where β is equal to x, y or z. Experiments (filled symbols) and DNS (empty symbols) are reported. Here, $S_{\partial\theta/\partial x}$ is shown by ● and ○, $S_{\partial\theta/\partial y}$ is shown by ■ and □, and $S_{\partial\theta/\partial z}$ is shown by ▲ and △. The vertical line indicates the transverse location of the source.

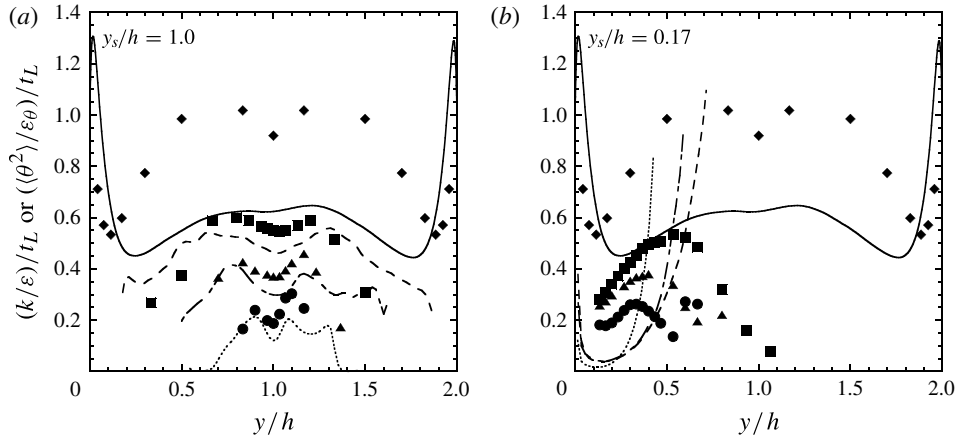

FIGURE 26. Transverse profiles of the mechanical and thermal time scales normalized by t_L. The lines are DNS results and the symbols are experimental ones. Here, $(k/\varepsilon)/t_L$ is shown by a solid line or ♦, $(\langle\theta^2\rangle/\varepsilon_\theta)/t_L$ at $t/t_L = 0.08$ is shown by a dotted line or ●, $(\langle\theta^2\rangle/\varepsilon_\theta)/t_L$ at $t/t_L = 0.2$ is shown by a dot-dashed line or ▲ and $(\langle\theta^2\rangle/\varepsilon_\theta)/t_L$ at $t/t_L = 0.4$ is shown by a dashed line or ■.

developed flow. We first remark that t_L is directly related to the mechanical time scale, $k/\varepsilon \equiv 1/2\langle u_i u_i\rangle/2\nu\langle s_{ij}s_{ij}\rangle \approx 3/2u_{rms}^2/(u_{rms}^3/\ell) \sim \ell/u_{rms} \sim h/u_{rms} = t_L$. Thus, it is reasonable for k/ε and t_L to be of the same order, which we observe (quite closely for the experiments, and within a factor of ∼1.5 for the simulations). This difference is due to the fact that, in the above approximation, $C_\varepsilon(\equiv \varepsilon/(u_{rms}^3/\ell))$ is not a constant but a decreasing function of the Reynolds number – in the range of moderate Reynolds numbers characterizing the present work, Sreenivasan (1984), Donzis, Sreenivasan & Yeung (2005) – such that $k/\varepsilon \sim C_\varepsilon t_L$ before C_ε has reached its asymptotic value.

Given this, one can conclude that isotropization of the scalar field occurs, more or less, within a few tenths of the mechanical time scale, implying that it may not be the most relevant scale. With respect to the thermal time scale, we remark that because $t_L \approx k/\varepsilon$, $(\langle\theta^2\rangle/\varepsilon_\theta)/t_L$ can be interpreted as a thermal-to-mechanical time scale ratio. In the present work, we observe that the thermal time scale is initially notably smaller than the mechanical one, of the same order as the return-to-isotropy time scale, namely tenths of t_L. It then increases with downstream distance, tending towards $(k/\varepsilon)/t_L$, except near the wall in the simulations. In the other cases, the increase in $(\langle\theta^2\rangle/\varepsilon_\theta)/t_L$ is consistent with a plume injected at small scales, which proceeds to grow and, ultimately, occupy the entire cross-section of the channel, taking on a time scale similar to that of the hydrodynamic field. However, near the wall for the simulations, which are at a lower Reynolds number than the experiments, we observe $(\langle\theta^2\rangle/\varepsilon_\theta)/t_L$ to be roughly independent of t/t_L. This observation is consistent with the notion that close to the wall, at low Reynolds numbers, another phenomenon is dictating the mixing process. As we shall argue shortly, it is most likely that this phenomenon is the production of ε_{θ_y} due to the mean velocity gradient, which is presumably controlling the thermal time scale and may explain why $(\langle\theta^2\rangle/\varepsilon_\theta)/t_L$ is not evolving with the downstream distance (t/t_L) in that region. However, when isotropization occurs, $(\langle\theta^2\rangle/\varepsilon_\theta)/t_L$ appears to increase, possibly asymptoting to $(k/\varepsilon)/t_L$. We also note that Rosset *et al.* (2001) and Gonzalez & Paranthoën (2003) argued that the thermal time scale may be more relevant to the mixing/isotropization process than the mechanical one. Furthermore, Gonzalez & Paranthoën (2003) noted that $(\langle\theta^2\rangle/\varepsilon_\theta) \sim (\ell_\theta/k_\theta^{1/2})$, where k_θ represents the kinetic energy of the flow structures of size ℓ_θ, which, in this case, falls between the Kolmogorov and integral length scales. Thus, $\ell_\theta/k_\theta^{1/2}$ can also be interpreted as a time scale related to the (inverse of the) vorticity at the scale ℓ_θ. Lastly, we observe a reasonable agreement between the experimental and numerical results for the thermal time scale in the case of the results for the centreline source. Near the wall, the difference may be due to the larger effect (in this region) of the difference in Reynolds numbers between the two sets of data, as already noted.

To further study the return to isotropy (or the lack of a return, in the case of the simulations of the plume emitted from a near-wall source), we consider the evolution equation of the scalar dissipation rate, given by

$$\begin{aligned}\frac{\partial\varepsilon_\theta}{\partial t} + \langle U_j\rangle\frac{\partial\varepsilon_\theta}{\partial x_j} = {} & \overbrace{-2\alpha\frac{\partial\langle U_j\rangle}{\partial x_i}\left\langle\frac{\partial\theta}{\partial x_i}\frac{\partial\theta}{\partial x_j}\right\rangle}^{\mathscr{P}} - 2\alpha\frac{\partial\langle T\rangle}{\partial x_j}\left\langle\frac{\partial u_j}{\partial x_i}\frac{\partial\theta}{\partial x_i}\right\rangle \\ & - 2\alpha\left\langle u_j\frac{\partial\theta}{\partial x_i}\right\rangle\frac{\partial^2\langle T\rangle}{\partial x_i\partial x_j} - 2\alpha\left\langle\frac{\partial u_j}{\partial x_i}\frac{\partial\theta}{\partial x_i}\frac{\partial\theta}{\partial x_j}\right\rangle \\ & + \frac{\partial}{\partial x_j}\left(\alpha\frac{\partial\langle\varepsilon_\theta\rangle}{\partial x_j} - \langle u_j\varepsilon_\theta\rangle\right) - \underbrace{2\alpha^2\left\langle\frac{\partial^2\theta}{\partial x_i\partial x_j}\frac{\partial^2\theta}{\partial x_i\partial x_j}\right\rangle}_{\Gamma},\end{aligned} \tag{7.1}$$

where repeated indices imply Einstein's summation convention. In the limit of large Reynolds and Péclet numbers, it is hypothesized (Corrsin 1953; Tennekes & Lumley 1972) that the above equation simplifies to a balance between the production of ε_θ due to stretching of the scalar gradients by the turbulent strain rate $(2\alpha\langle(\partial u_i/\partial x_i)(\partial\theta/\partial x_i)(\partial\theta/\partial x_j)\rangle)$ and the destruction of ε_θ by molecular processes $(\Gamma = 2\alpha^2\langle(\partial^2\theta/\partial x_i\partial x_j)(\partial^2\theta/\partial x_i\partial x_j)\rangle)$. However, at finite Reynolds and Péclet numbers,

other terms may be relevant. To investigate and explain the previously observed anisotropy, we focus on the two terms $\mathscr{P}$ $(=\mathscr{P}_x+\mathscr{P}_y+\mathscr{P}_z)$ and Γ $(=\Gamma_x+\Gamma_y+\Gamma_z)$. The former is the production of ε_θ by mean velocity gradients and the latter quantifies the dissipation of ε_θ by molecular processes, as just noted. For channel flow, the components of these two terms are $\mathscr{P}=\mathscr{P}_y=-2\alpha\partial\langle U\rangle/\partial y\langle(\partial\theta/\partial y)(\partial\theta/\partial x)\rangle$ with $\mathscr{P}_x=\mathscr{P}_z=0$ and $\Gamma_x=2\alpha^2[\langle(\partial^2\theta/\partial x^2)^2\rangle+\langle(\partial^2\theta/\partial x\partial y)^2\rangle+\langle(\partial^2\theta/\partial x\partial z)^2\rangle]$, $\Gamma_y=2\alpha^2[\langle(\partial^2\theta/\partial y\partial x)^2\rangle+\langle(\partial^2\theta/\partial y^2)^2\rangle+\langle(\partial^2\theta/\partial y\partial z)^2\rangle]$ and $\Gamma_z=2\alpha^2[\langle(\partial^2\theta/\partial z\partial x)^2\rangle+\langle(\partial^2\theta/\partial z\partial y)^2\rangle+\langle(\partial^2\theta/\partial z^2)^2\rangle]$. Figure 27 shows the wall-normal profiles of the three components of Γ and $\mathscr{P}_y$ for the two source locations ($y_s/h=1.0$ and 0.17) at two downstream positions ($t/t_L=0.08$ and 0.4). It should be noted that the y and z components of Γ were not accessible experimentally as $\partial\theta/\partial y$ and $\partial\theta/\partial z$ were not simultaneously measured. Furthermore, combined statistical moments of both the velocity and temperature derivatives were not computed due to the fact that the velocity and temperature field were not calculated or measured simultaneously in the present approach. This thus precludes any comparison of $\mathscr{P}$ with the other leading-order term in (7.1).

The mean velocity gradient that only exists in the wall-normal direction contributes to the production of ε_θ (in the y direction). The relative importance of this production depends on the wall-normal location within the channel. As the mean velocity gradient $(\partial\langle U\rangle/\partial y)$ is small in the centre of the channel, there is very little production of scalar dissipation by the mean velocity field in the central region (and none at the channel midplane, by symmetry). However, the contribution of $\mathscr{P}_y$ to ε_{θ_y} is not negligible in the near-wall region, as the velocity gradients are large there. In fact, figure 27 showsthat the production of dissipation in the wall-normal direction is of the same order of magnitude as Γ_y near the walls. The figure also shows that $\mathscr{P}_y$ does not contribute to the evolution of ε_{θ_y} (or ε_θ) when the source is at the centreline, as expected. Lastly, this production of ε_θ due to mean velocity gradients now explains the aforementioned (i) persistent anisotropies for the near-wall scalar fields (figure 24) and (ii) persistence of a maximum in ε_{θ_y} near the wall (figure 20). In addition, it may possibly explain the constancy of the thermal time scale near the wall, when $y_s/h=0.17$, as observed in figure 26(*b*). Johansson & Wikström (1999) performed DNS of turbulent channel flow with an imposed mean scalar gradient. In the near-wall region, they showed that the two mean gradient production terms (i.e. the first and second terms on the right-hand side of (7.1)) as well as the term that is the scalar-field analogue to the vortex-stretching term in the turbulent enstrophy budget (i.e. the fourth term on the right-hand side of (7.1)) contribute the most to the production of ε_θ. These results agree with those presented herein.

Anisotropy-invariant maps for ε_θ (Antonia & Kim 1994) are plotted in figures 28–30, where the three solid lines are (often referred to as) the Lumley triangle (Lumley 1978). This triangle is delimited by the following three curves (in the (III, −II) plane):

$$\mathrm{III}=-\tfrac{\mathrm{II}}{3}-\tfrac{1}{27}, \tag{7.2}$$

$$\mathrm{III}=-2\left(\tfrac{\mathrm{II}}{3}\right)^{3/2}, \tag{7.3}$$

$$\mathrm{III}=2\left(\tfrac{\mathrm{II}}{3}\right)^{3/2}. \tag{7.4}$$

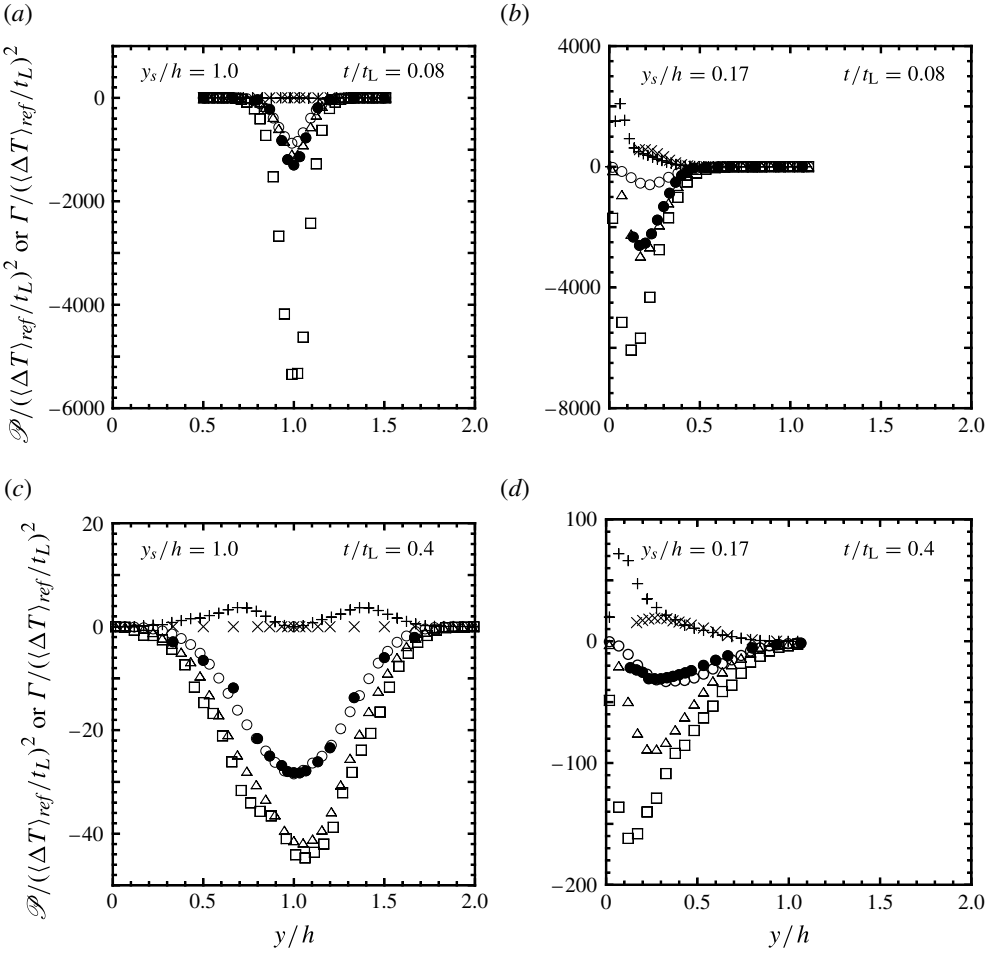

FIGURE 27. The wall-normal evolution of the y-component of the production of ε_θ by the mean velocity gradient and the three components of the dissipation of ε_θ. The experimental results are denoted by the filled symbols ($-2\alpha^2\big(\langle(\partial^2\theta/\partial x^2)^2\rangle + \langle(\partial^2\theta/\partial x\partial y)^2\rangle + \langle(\partial^2\theta/\partial x\partial z)^2\rangle\big)$ (●)) and the numerical results are denoted by the empty symbols ($-2\alpha^2[\langle(\partial^2\theta/\partial x^2)^2\rangle + \langle(\partial^2\theta/\partial x\partial y)^2\rangle + \langle(\partial^2\theta/\partial x\partial z)^2\rangle]$ (○), $-2\alpha^2[\langle(\partial^2\theta/\partial y\partial x)^2\rangle + \langle(\partial^2\theta/\partial y^2)^2\rangle + \langle(\partial^2\theta/\partial y\partial z)^2\rangle]$ (□) and $-2\alpha^2[\langle(\partial^2\theta/\partial z\partial x)^2\rangle + \langle(\partial^2\theta/\partial z\partial y)^2\rangle + \langle(\partial^2\theta/\partial z^2)^2\rangle]$ (△)). The production of dissipation $-2\alpha\langle U\rangle_y\langle(\partial\theta/\partial y)(\partial\theta/\partial x)\rangle$ is also reported for the experiments (×) and the DNS (+).

Here, II and III are the second and third invariants of the scalar dissipation rate anisotropy tensor defined as

$$t_{ij} = \alpha\frac{\left\langle \dfrac{\partial\theta}{\partial x_i}\dfrac{\partial\theta}{\partial x_j}\right\rangle}{\langle\varepsilon_\theta\rangle} - \frac{1}{3}\delta_{ij}, \tag{7.5}$$

where δ_{ij} is the Kronecker delta. The second and third invariants are given by

$$\mathrm{II} = -\tfrac{1}{2}t_{ij}t_{ji}, \tag{7.6}$$

$$\mathrm{III} = \tfrac{1}{3}t_{ij}t_{jk}t_{ki}. \tag{7.7}$$

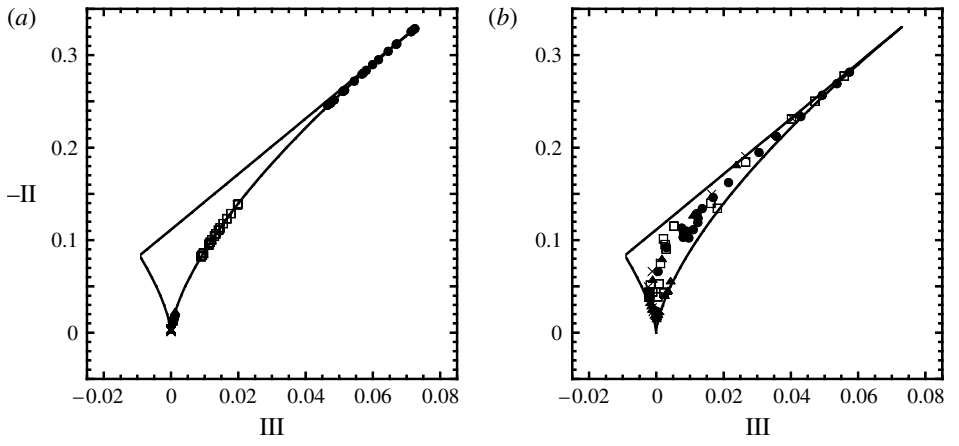

FIGURE 28. Anisotropy-invariant map of ε_θ for $y_s/h = 1.0$ (a) and $y_s/h = 0.17$ (b). Statistics were computed at $t/t_L = 0.02$ (○), 0.08 (□), 0.2 (△) and 0.4 (×) and for $y/h \in [0.8, 1.2]$ (a) and $y/h \in [0.0, 0.4]$ (b).

The plot of $-$II versus III represents all the possible states that characterize the tensor t_{ij}. Curves (7.3) and (7.4) are respectively the right and left 'axisymmetric' boundaries of the anisotropy-invariant map. The vertex II = III = 0 characterizes the isotropic state. The top right vertex of the line given by (7.2) represents the one-component state and the bottom left vertex represents the two-component state.

The return to isotropy behind a centreline source (figure 28a) is (i) clearly axisymmetric, consistent with the previous results of figure 23, and (ii) more rapid than that of the scalar field behind the near-wall source. The axisymmetry of the scalar field behind the centreline line source is more clearly observed in figure 29, which shows a very large level of axisymmetry at $y/h = 1.0$, but a slightly smaller degree of axisymmetry at $y/h = 0.8$. These results should be contrasted with those of figure 30, which depicts the anisotropy-invariant maps for different wall-normal locations for the scalar field generated by the near-wall source. Of particular interest is the evolution from a one-dimensional state very close to the wall (Antonia & Kim 1994) in figure 30(c) to an almost axisymmetric state farther away from the wall in figure 30(d).

7.4. *Conditional statistics*

To gain further insight into the dependence of the scalar dissipation rate, ε_θ, on the scalar fluctuations, θ, which is of particular use in p.d.f. models of scalar mixing, we examine the expectation of $\varepsilon_{\theta_\beta}$ conditioned on individual values of θ, i.e. $\langle \varepsilon_{\theta_\beta} | \theta \rangle$, where $\varepsilon_{\theta_\beta}$ is the β-component of the scalar dissipation ($\beta = x$, y or z). Theoretical work has shown that the form of the conditional expectation profiles, $\langle \varepsilon_\theta | \theta \rangle$, depends on the p.d.f. of the scalar fluctuation, θ (Pope & Ching 1993). A Gaussian p.d.f. of θ is associated with ε_θ and θ being independent. In this case, $\langle \varepsilon_\theta | \theta \rangle$ is found to be a constant (e.g. Anselmet, Djeridi & Fulachier 1994, figure 9b). A super-Gaussian p.d.f. of the scalar is associated with a rounded concave-up V-shape for the profile (Sinai & Yakhot 1989; Jayesh & Warhaft 1992), whereas a sub-Gaussian p.d.f. is associated with a rounded concave-down V-shape for the profile (Mydlarski 2003).

In figure 31(a,c) the expected values of the various components of the scalar dissipation rate conditioned on the temperature fluctuations are plotted for $y_s/h = 1.0$.

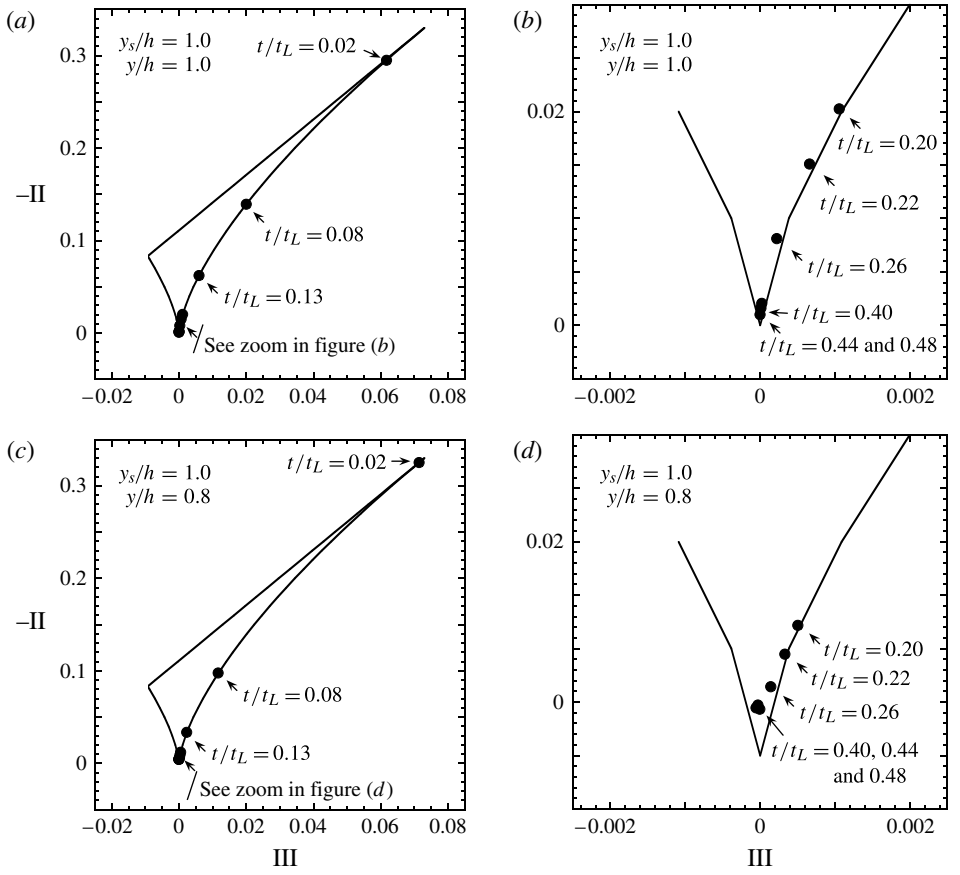

FIGURE 29. Anisotropy-invariant maps of ε_θ. A close-up of figure (*a*) is presented in figure (*b*). A close-up of figure (*c*) is presented in figure (*d*). Statistics were computed from $t/t_L = 0.02$ to 0.48.

In the present work, the scalar dissipation rate conditioned on the scalar fluctuation exhibits a concave-down rounded V-shape. Such a shape indicates that large values of the scalar fluctuation are associated with low values of the scalar dissipation. Each plot begins with an approximately linear departure from $\theta/\theta_{rms} \approx -1.5$, increasing to a maximum, after which the conditional expectation begins to decrease. The double peaks of $\langle \varepsilon_{\theta_y} | \theta \rangle$ measured in the experiments in the vicinity of the source disappear farther downstream. These may be related to the previously discussed p.d.f.s of $\partial\theta/\partial y$, which were shown to be bi- or trimodal near the source (see figure 16).

In figure 31(*b*,*d*) the conditional expectation $\langle \varepsilon_{\theta_\beta} | \theta/\theta_{rms} \rangle / \langle \varepsilon_{\theta_\beta} \rangle$ is plotted when the line source is near the wall ($y_s/h = 0.17$). The general form of the profiles is somewhat different from that with the centreline line source. In contrast to the DNS profiles, the experimental profiles increase near the upper limits of the range of temperature fluctuation. This increase also appears when the source is at the centreline but with a (relatively) smaller magnitude. It should be noted that figure 31(*d*) has been plotted with different axis ranges due to large rare excursions in this part of the flow, where some measurements are outside the plume and the others in its outer edges.

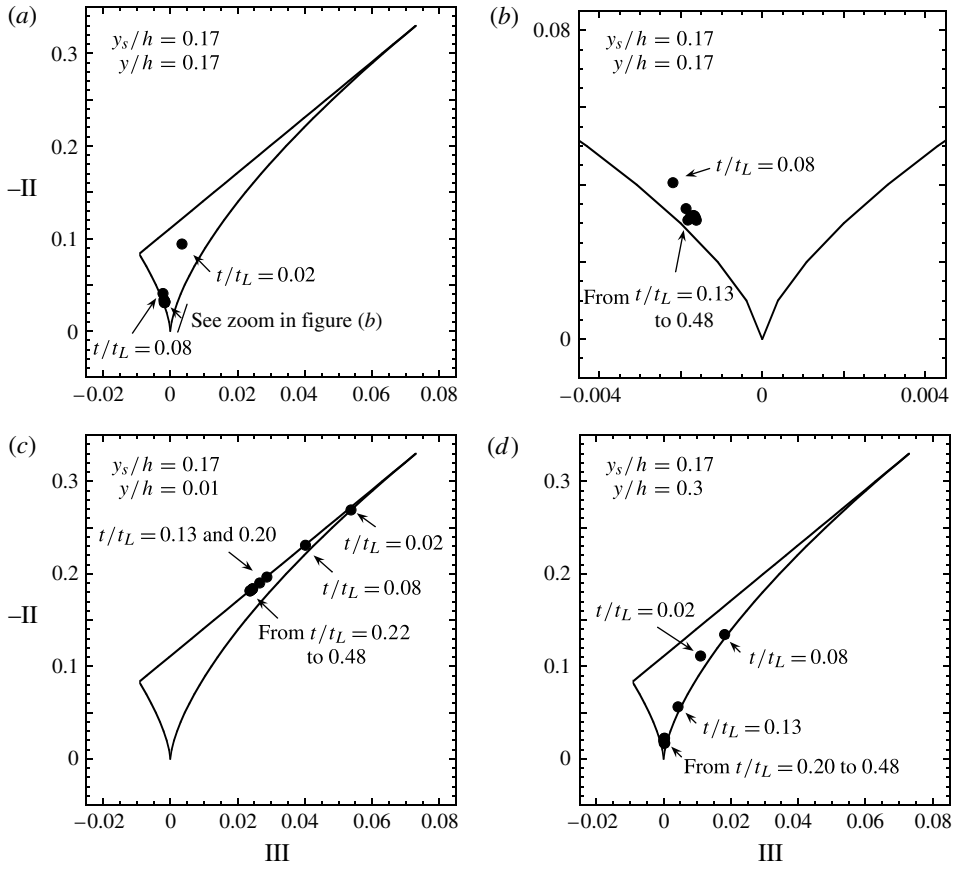

FIGURE 30. Anisotropy-invariant maps of ε_θ. A close-up of figure (*a*) is presented in figure (*b*). Statistics were computed from $t/t_L = 0.02$ to 0.48.

Kailasnath, Sreenivasan & Saylor (1993) investigated the conditional scalar dissipation rate in three different shear flows, wakes, jets and the atmospheric surface layer. They also found that the 'hot side' of the conditional expectation $\langle \varepsilon_\theta | \theta \rangle$ increased with θ. They concluded that the very hot events associated with very high intermittent dissipation rates were non-universal. In addition, they mentioned that the low-temperature events may also be non-universal but their contribution to the conditional expectation is small because the dissipation in the cold fluid is small. These observations are consistent with the present results.

Independently of the source location, figure 31 shows a tendency to isotropic behaviour as the downstream distance from the source increases. At low θ/θ_{rms}, the experiments and DNS agree relatively well. However, the discrepancies at large θ/θ_{rms} may be due to the fact that large positive fluctuations of θ are rare and may suffer from a reduced level of statistical convergence.

The expectations of the components of the dissipation conditioned upon individual values of the temperature derivatives, $\langle \varepsilon_{\theta_\beta} | \partial\theta/\partial x \rangle$, where $\beta = x$, y or z, are plotted in figure 32 for the two line source locations presented herein. These figures show that larger magnitudes of $\partial\theta/\partial x$ lead to higher values of ε_{θ_x} consistent with the definition $\varepsilon_{\theta_x} \equiv \alpha \langle (\partial\theta/\partial x)^2 \rangle$. In addition, ε_{θ_y} and ε_{θ_z} do not directly depend on $\partial\theta/\partial x$, which

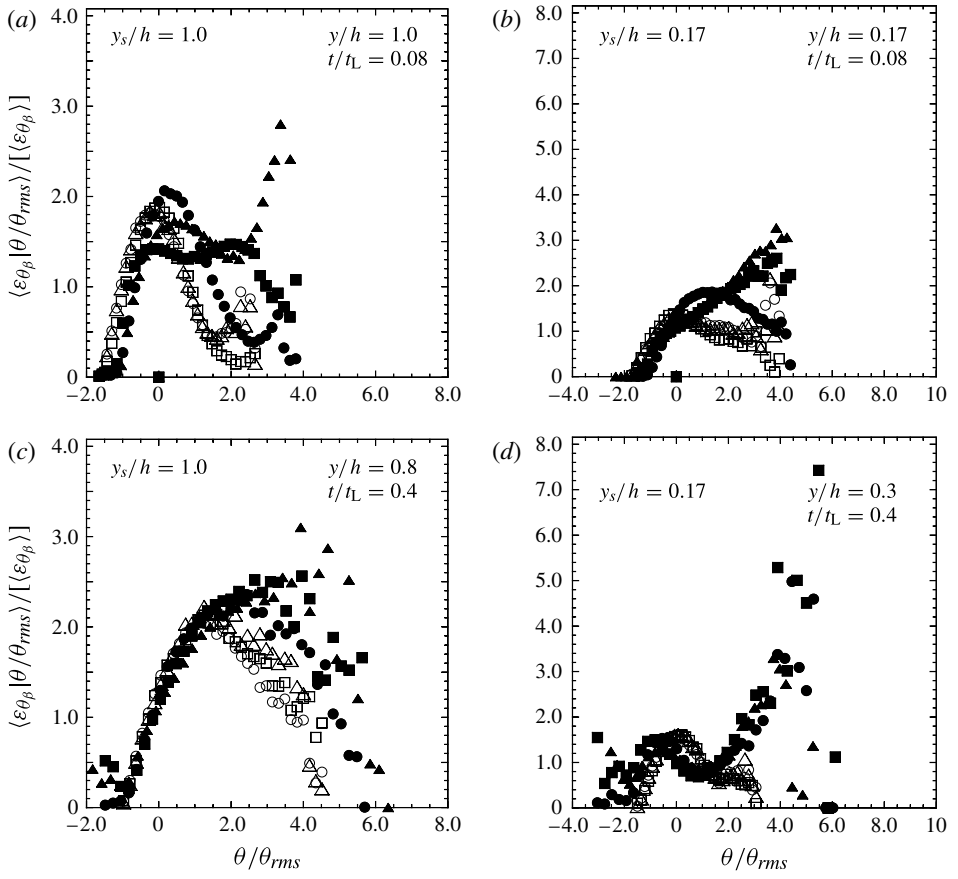

FIGURE 31. The expectation of the components of the temperature dissipation conditioned on the temperature fluctuations. The experimental results are denoted by the filled symbols ($\langle \varepsilon_{\theta_x} | \theta \rangle$ (●), $\langle \varepsilon_{\theta_y} | \theta \rangle$ (■) and $\langle \varepsilon_{\theta_z} | \theta \rangle$ (▲)) and the numerical results are denoted by the empty symbols ($\langle \varepsilon_{\theta_x} | \theta \rangle$ (○), $\langle \varepsilon_{\theta_y} | \theta \rangle$ (□) and $\langle \varepsilon_{\theta_z} | \theta \rangle$ (△)).

explains the flatter profiles obtained for $\langle \varepsilon_{\theta_y} | \partial\theta/\partial x \rangle$ and $\langle \varepsilon_{\theta_z} | \partial\theta/\partial x \rangle$. That being said, they are clearly not independent, especially farther downstream. Overall, a good agreement between experiments and DNS is observed.

Figures 33 and 34 compare the expectations of $\varepsilon_{\theta_\beta}$ conditioned upon individual values of $\partial\theta/\partial x$, $\partial\theta/\partial y$ and $\partial\theta/\partial z$. The figures show consistent results for all three components, where (i) the correlation is highest when considering the component of ε_θ and the derivative of θ measured in the same direction and (ii) a reduced, but clearly non-zero, correlation is observed for the expectations conditioned on the temperature derivative in a different direction.

8. Conclusions

In the present work, the dissipation rate of a scalar (temperature) emitted from a concentrated line source in a fully developed turbulent channel flow was studied by means of both experiments and numerical simulations. The aim was to investigate the evolution of the small scales of the scalar field by measuring the (three components

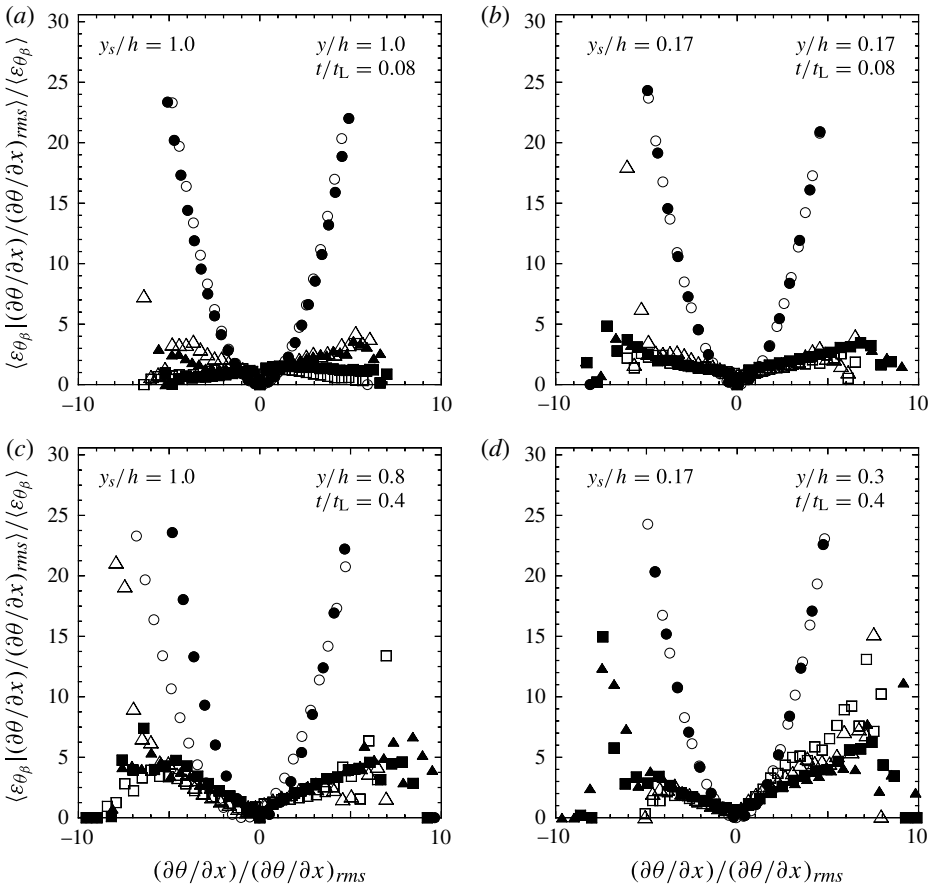

FIGURE 32. The expectation of the components of the temperature dissipation conditioned on the x partial derivative of the temperature fluctuations. The experimental results are denoted by the filled symbols ($\langle \varepsilon_{\theta_x} | \partial\theta/\partial x \rangle$ (●), $\langle \varepsilon_{\theta_y} | \partial\theta/\partial x \rangle$ (■) and $\langle \varepsilon_{\theta_z} | \partial\theta/\partial x \rangle$ (▲)) and the numerical results are denoted by the empty symbols ($\langle \varepsilon_{\theta_x} | \partial\theta/\partial x \rangle$ (○), $\langle \varepsilon_{\theta_y} | \partial\theta/\partial x \rangle$ (□) and $\langle \varepsilon_{\theta_z} | \partial\theta/\partial x \rangle$ (△)).

of the) scalar dissipation rate, ε_θ, at several downstream and wall-normal locations. The scalar was injected in a highly anisotropic manner and an examination of the downstream evolution of ε_θ permitted an investigation of the return to isotropy of the small scales of the scalar field.

The large- and small-scale statistics of the scalar field were reported for two different source locations ($y_s/h = 1.0$ and 0.17), with an emphasis on the small-scale ones, given the nature of this study. Overall, a good agreement between the experimental and numerical data was obtained, confirming that the DNS is capable of resolving the experimentally measured dissipative scales. Some discrepancies between the two were, however, observed. These were attributed to the differences in the Reynolds number between the experiments ($Re_\tau = 520$) and the DNS ($Re_\tau = 190$).

The principal contribution of this work is a detailed description of the downstream and transverse evolutions of the small-scale statistics of the scalar field (with an emphasis on the scalar dissipation rate), as well as their dependence on the source location. The effect of the source location is a critical aspect of the present work, as

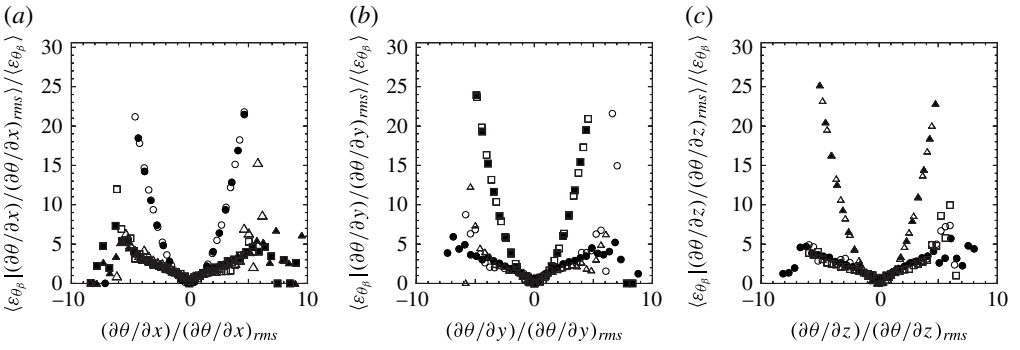

FIGURE 33. The expectation of the components of the temperature dissipation conditioned on the x, y and z partial derivatives of the temperature fluctuations for $y_s/h = 1.0$ at $t/t_L = 0.4$ and $y/h = 1.0$. The experimental results are denoted by the filled symbols and the numerical results are denoted by the empty symbols. (*a*) $\langle \varepsilon_{\theta_\beta} | \partial\theta/\partial x \rangle$. (*b*) $\langle \varepsilon_{\theta_\beta} | \partial\theta/\partial y \rangle$. (*c*) $\langle \varepsilon_{\theta_\beta} | \partial\theta/\partial z \rangle$. Here, $\beta = x$ (circles), $\beta = y$ (squares) and $\beta = z$ (triangles).

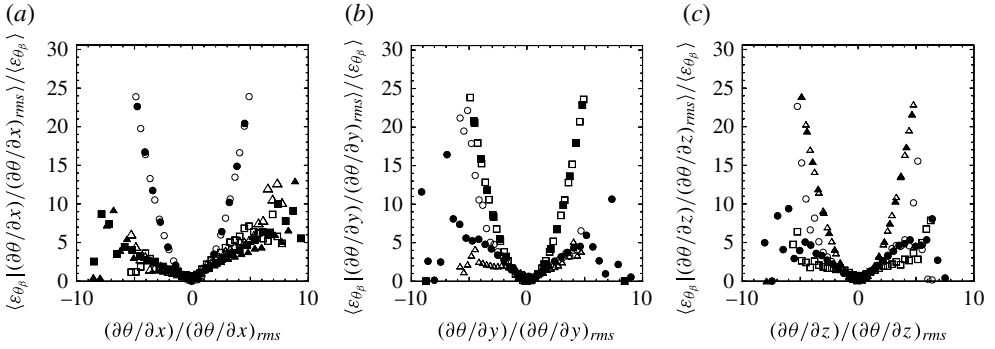

FIGURE 34. The expectation of the components of the temperature dissipation conditioned on the x, y and z partial derivatives of the temperature fluctuations for $y_s/h = 0.17$ at $t/t_L = 0.4$ and $y/h = 0.17$. The experimental results are denoted by the filled symbols and the numerical results are denoted by the empty symbols. (*a*) $\langle \varepsilon_{\theta_\beta} | \partial\theta/\partial x \rangle$. (*b*) $\langle \varepsilon_{\theta_\beta} | \partial\theta/\partial y \rangle$. (*c*) $\langle \varepsilon_{\theta_\beta} | \partial\theta/\partial z \rangle$. Here, $\beta = x$ (circles), $\beta = y$ (squares) and $\beta = z$ (triangles).

it is an essential parameter that is only present in inhomogeneous flows, a category into which all practical flows fall. The present work provides insight into the effect of source location on the small-scale statistics of the scalar field, which, until now, had not been explicitly studied.

To this end, the downstream and transverse evolutions of the spectra and p.d.f.s of the scalar gradients ($\partial\theta/\partial x_\beta$), ε_{θ_x}, ε_{θ_y}, ε_{θ_z} and ε_θ, as well as their dependence on the source location, were analysed. For the case of the centreline source, a tendency for these statistics to return to isotropy was always observed. When the source was located near the wall, the tendency to return to isotropy was not as evident, given that the production of ε_{θ_y} due to the mean velocity gradient, which was most evident in plots of $\varepsilon_{\theta_\beta}/\varepsilon_{\theta_\gamma}$, may be non-negligible at lower Reynolds numbers, such as those which characterized our numerical simulations. Because the near-wall region has characteristics that both reduce the anisotropy (e.g. higher degrees of mixing, due to the more intense nature of the turbulence therein) and increase the

anisotropy (e.g. production of ε_{θ_y} by mean velocity gradients), the dependence of the return to isotropy on the source location is complex, in addition to possibly being dependent on the Reynolds number, the Schmidt number (e.g. Yeung, Xu & Sreenivasan 2002; Brethouwer, Hunt & Nieuwstadt 2003), etc. We have also argued that when the production of ε_{θ_y} by mean velocity gradients is non-negligible, a return to isotropy is inhibited by this mechanism, which possibly maintains the thermal time scale at a fixed value, unlike what was observed when small-scale isotropy of the scalar field was recovered. The return to isotropy of the scalar field was also quantified using anisotropy-invariant maps for the scalar dissipation rate, which highlighted, downstream of the centreline source, (i) the axisymmetric nature of the scalar dissipation rate and (ii) an improved tendency towards isotropy of the small scales. The nature of the anisotropy-invariant maps was, however, distinctly different in the near-wall region, varying from a one-dimensional state very close to the wall towards an axisymmetric state as the centreline was approached. Lastly, the conditional expectations of the three components of ε_θ were presented, which, in addition to providing insight into the structure of the scalar field, should be of benefit to those developing mixing models for p.d.f. methods.

The more rapid return to isotropy of certain statistics (e.g. both the spectra and p.d.f.s of the scalar gradients, the p.d.f.s of ε_θ, etc.) in the near-wall region is consistent with the scalar field undergoing increased mixing in regions of more intense turbulence (i.e. regions of locally higher turbulent Reynolds numbers). However, in the current flow, the increased values of u_{rms} are associated with the larger contribution of the production of turbulent kinetic energy by mean velocity gradients, which, as previously noted, also serves to produce anisotropy. Increased mixing in regions or more intense turbulence is consistent with the arguments of Rosset *et al.* (2001) and Gonzalez & Paranthoën (2003), as increased levels of turbulence can be associated with increased vorticity. Rosset *et al.* (2001) hypothesized that the return to isotropy in a flow in which the scalar field is injected at small scales is caused by both molecular dissipation and stretching, in which the latter is effected by both strain and rotation, with rotation serving to reorient the scalar gradients and thus 'isotropizing' the scalar field. Gonzalez & Paranthoën (2003) further analysed the work of Rosset *et al.* (2001) and suggested that the return to isotropy was 'governed by vorticity at scales of the order of the instantaneous scalar sheet thickness', arguing that vorticity at smaller scales could not significantly distort the plume, whereas that at large scales would be able to rotate the plume, but would be weaker (assuming typical Kolmogorov arguments for the dependence of the vorticity on the length scale).

In addition to the above, it is worth reiterating the comments of Rosset *et al.* (2001) and Gonzalez & Paranthoën (2003), who emphasized that flows in which the scalar is injected at small scales are notably different from those in which the scalar is injected at large scales (i.e. by way of a mean scalar gradient). In the latter class of flows, anisotropy is continually generated by the large-scale anisotropic injection mechanism. In the current case of small-scale injection by a line (or point) source, the small-scale anisotropy does not originate from large-scale anisotropy being transferred to smaller scales, because it originates at small scales, and the mean scalar gradients, which are the source of the anisotropy, become smaller and smaller as the plume is increasingly well mixed, thus also promoting, in part, a return to isotropy. Nevertheless, the exact nature of the return to isotropy of a scalar field injected at small scales merits additional investigation, such as (i) investigation that might focus on the effect of the intensity of the turbulence/local Reynolds number, without compounding the results with a change in the mean velocity gradient/production of

turbulent kinetic energy, (ii) further investigation of the effect of the Schmidt number or (iii) numerical simulations in which simultaneous small-scale velocity and scalar statistics can be recorded, because experimental measurement of all three scalar gradients and all nine velocity ones remains an exceedingly difficult task.

Acknowledgement

The authors acknowledge the gracious support of the Natural Sciences and Engineering Research Council of Canada.

REFERENCES

ABE, H., KAWAMURA, H. & MATSUO, Y. 2001 Direct numerical simulation of a fully developed turbulent channel flow with respect to the Reynolds number dependence. *J. Fluid. Eng. - T. ASME* **123**, 382–393.

ABE, H., KAWAMURA, H. & MATSUO, Y. 2004 Surface heat-flux fluctuations in a turbulent channel flow up to $Re_\tau = 1020$ with $Pr = 0.025$ and 0.71. *Intl J. Heat Fluid Flow* **25**, 404–419.

ANSELMET, F., DJERIDI, H. & FULACHIER, L. 1994 Joint statistics of a passive scalar and its dissipation in turbulent flows. *J. Fluid Mech.* **280**, 173–197.

ANSELMET, F., DJERIDI, H. & FULACHIER, L. 1997 Simultaneous measurements of temperature and its dissipation using pairs of parallel cold wires. *Exp. Fluids* **23**, 177–186.

ANTONIA, R. A. & BROWNE, L. W. B. 1986 Anisotropy of the temperature dissipation in a turbulent wake. *J. Fluid Mech.* **163**, 393–403.

ANTONIA, R. A. & KIM, J. 1994 A numerical study of local isotropy of turbulence. *Phys. Fluids* **6**, 834–841.

ANTONIA, R. A., KIM, J. & BROWNE, L. W. B. 1991 Some characteristics of small-scale turbulence in a turbulent duct flow. *J. Fluid Mech.* **233**, 369–388.

ANTONIA, R. A. & MI, J. 1993 Temperature dissipation in a turbulent round jet. *J. Fluid Mech.* **250**, 531–551.

BAKOSI, J., FRANZESE, P. & BOYBEYI, Z. 2007 Probability density function modeling of scalar mixing from concentrated sources in turbulent channel flow. *Phys. Fluids* **19**, 115106.

BALSARA, D. S. 2001 Divergence-free adaptive mesh refinement for magnetohydrodynamics. *J. Comput. Phys.* **174**, 614–648.

BOPPANA, V. B. L., XIE, Z. T. & CASTRO, I. P. 2012 Large-eddy simulation of dispersion from line sources in a turbulent channel flow. *Flow Turbul. Combust.* **88**, 311–342.

BRETHOUWER, G., BOERSMA, B. J., POURQUIE, M. & NIEUWSTADT, F. T. M. 1999 Direct numerical simulation of turbulent mixing of a passive scalar in pipe flow. *Eur. J. Mech. (B/Fluids)* **18**, 739–756.

BRETHOUWER, G., HUNT, J. C. R. & NIEUWSTADT, F. T. M. 2003 Micro-structure and Lagrangian statistics of the scalar field with a mean gradient in isotropic turbulence. *J. Fluid Mech.* **474**, 193–225.

CHAMECKI, M., MENEVEAU, C. & PARLANGE, M. B. 2008 A hybrid spectral/finite-volume algorithm for large-eddy simulation of scalars in the atmospheric boundary layer. *Boundary-Layer Meteorol.* **128**, 473–484.

CHUNG, M. K. & KYONG, N. H. 1989 Measurement of turbulent dispersion behind a fine cylindrical heat source in a weakly sheared flow. *J. Fluid Mech.* **205**, 171–193.

CLYNE, J., MININNI, P., NORTON, A. & RAST, M. 2007 Interactive desktop analysis of high resolution simulations: application to turbulent plume dynamics and current sheet formation. *New J. Phys.* **9**, 301.

CLYNE, J. & RAST, M. 2005 A prototype discovery environment for analyzing and visualizing terascale turbulent fluid flow simulations. In *EProc. Visualization and Data Analysis 2005* pp. 284–294.

CORRSIN, S. 1951 On the spectrum of isotropic temperature fluctuations in an isotropic turbulence. *J. Appl. Phys.* **22**, 469–473.

CORRSIN, S. 1952 Heat transfer in isotropic turbulence. *J. Appl. Phys.* **23**, 113–118.

CORRSIN, S. 1953 Remarks on turbulent heat transfer *Proceedings of Iowa Thermodynamics Symposium, State University of Iowa, Iowa City* pp. 5–30.

COSTA-PATRY, E. & MYDLARSKI, L. 2008 Mixing of two thermal fields emitted from line sources in turbulent channel flow. *J. Fluid Mech.* **609**, 349–375.

DAHM, W. J. A. & BUCH, K. A. 1989 Lognormality of the scalar dissipation pdf in turbulent flows. *Phys. Fluids* A **1**, 1290–1293.

DANAILA, L., ANTONIA, R. A. & BURATTINI, P. 2012 Comparison between kinetic energy and passive scalar energy transfer in locally homogeneous isotropic turbulence. *Physica* D **241**, 224–231.

DANAILA, L., ZHOU, T., ANSELMET, F. & ANTONIA, R. A. 2000 Calibration of a temperature dissipation probe in decaying grid turbulence. *Exp. Fluids* **28**, 45–50.

DONZIS, D. A., SREENIVASAN, K. R. & YEUNG, P. K. 2005 Scalar dissipation rate and dissipative anomaly in isotropic turbulence. *J. Fluid Mech.* **532**, 199–216.

FACKRELL, J. E. & ROBINS, A. G. 1982 Concentration fluctuations and fluxes in plumes from point sources in a turbulent boundary layer. *J. Fluid Mech.* **117**, 1–26.

GALANTUCCI, L. & QUADRIO, M. 2010 Very fine near-wall structures in turbulent scalar mixing. *Intl J. Heat Fluid Flow* **31**, 499–506.

GERMAINE, E., MYDLARSKI, L. & CORTELEZZI, L. 2013 3DFLUX: a high-order fully three-dimensional flux integral solver for the scalar transport equation. *J. Comput. Phys.* **240**, 121–144.

GIBSON, J. F. 2010 Channelflow: a spectral Navier–Stokes simulator in C++. *Tech. Rep.* University of New Hampshire.

GIBSON, J. F., HALCROW, J. & CVITANOVIĆ, P. 2008 Visualizing the geometry of state space in plane Couette flow. *J. Fluid Mech.* **611**, 107–130.

GONZALEZ, M. 2000 Study of the anisotropy of a passive scalar field at the level of dissipation. *Phys. Fluids* **12**, 2302–2310.

GONZALEZ, M. & PARANTHOËN, P. 2003 On the role of vorticity in the microstructure of a passive scalar field. *Phys. Fluids* **16**, 219–221.

GURVICH, A. S. & YAGLOM, A. M. 1967 Breakdown of eddies and probability distributions for small-scale turbulence. *Phys. Fluids* **10**, 59–65.

HOLZER, M. & SIGGIA, E. D. 1994 Turbulent mixing of a passive scalar. *Phys. Fluids* **6**, 1820–1837.

HUSSAIN, A. K. M. F. & REYNOLDS, W. C. 1975 Measurements in fully developed turbulent channel flow. *Trans. ASME J. Fluids Engng* **97**, 568–578.

INCROPERA, F. P., DE WITT, D. P., BERGMAN, T. L. & LAVINE, A. S. 2007 *Fundamentals of Heat and Mass Transfer*. 6th edn John Wiley and Sons Inc.

JAYESH & WARHAFT, Z. 1992 Probability distribution, conditional dissipation, and transport of passive temperature fluctuations in grid-generated turbulence. *Phys. Fluids* A **4**, 2292–2307.

JOHANSSON, A. V. & WIKSTRÖM, P. M. 1999 DNS and modelling of passive scalar transport in turbulent channel flow with a focus on scalar dissipation rate modelling. *Flow Turbul. Combust.* **63**, 223–245.

KAILASNATH, P., SREENIVASAN, K. R. & SAYLOR, J. R. 1993 Conditional scalar dissipation rates in turbulent wakes, jets, and boundary layers. *Phys. Fluids* A **5**, 3207–3215.

KARNIK, U. & TAVOULARIS, S. 1989 Measurements of heat diffusion from a continuous line source in a uniformly sheared turbulent flow. *J. Fluid Mech.* **202**, 233–261.

KAWAMURA, H., OHSAKA, K., ABE, H. & YAMAMOTO, K. 1998 DNS of turbulent heat transfer in channel flow with low to medium-high Prandtl number fluid. *Intl J. Heat Fluid Flow* **19**, 482–491.

KIM, J., MOIN, P. & MOSER, R. 1987 Turbulence statistics in fully developed channel flow at low Reynolds number. *J. Fluid Mech.* **177**, 133–166.

KOLMOGOROV, A. 1941 The local structure of turbulence in incompressible viscous fluid for very large Reynolds numbers. *Dokl. Akad. Nauk SSSR* **30**, 301–305.

KOZUKA, M., SEKI, Y. & KAWAMURA, H. 2009 DNS of turbulent heat transfer in a channel flow with a high spatial resolution. *Intl J. Heat Fluid Flow* **30**, 514–524.

LaRue, J. C. & Libby, P. A. 1981 Thermal mixing layer downstream of half-heated turbulence grid. *Phys. Fluids* **24**, 597–603.

Lavertu, R. A. & Mydlarski, L. 2005 Scalar mixing from a concentrated source in turbulent channel flow. *J. Fluid Mech.* **528**, 135–172.

Lemay, J. & Benaïssa, A. 2001 Improvement of cold-wire response for measurement of temperature dissipation. *Exp. Fluids* **31**, 347–356.

Lepore, J. & Mydlarski, L. 2011 Lateral dispersion from a concentrated line source in turbulent channel flow. *J. Fluid Mech.* **678**, 417–450.

Li, S. & Li, H. 2004 A novel approach of divergence-free reconstruction for adaptive mesh refinement. *J. Comput. Phys.* **199**, 1–15.

Livescu, D., Jaberi, F. A. & Madnia, C. K. 2000 Passive-scalar wake behind a line source in grid turbulence. *J. Fluid Mech.* **416**, 117–149.

Lockwood, F. C. & Moneib, H. A. 1980 Fluctuating temperature measurements in a heated round free jet. *Combust. Sci. Technol.* **22**, 63–81.

Lumley, J. L. 1978 Computational modeling of turbulent flows. *Adv. Appl. Mech.* **18**, 123–176.

Ma, B. K. & Warhaft, Z. 1986 Some aspects of the thermal mixing layer in grid turbulence. *Phys. Fluids* **29**, 3114–3120.

Moin, P. & Mahesh, K. 1998 Direct numerical simulation: a tool in turbulence research. *Annu. Rev. Fluid Mech.* **30**, 539–578.

Moser, R. D., Kim, J. & Mansour, N. N. 1999 Direct numerical simulation of turbulent channel flow up to $Re = 590$. *Phys. Fluids* **11**, 943–945.

Mydlarski, L. 2003 Mixed velocity-passive scalar statistics in high-Reynolds-number turbulence. *J. Fluid Mech.* **475**, 173–203.

Mydlarski, L., Danaila, L. & Lavertu, R. A. 2007 Isotropy of the temperature field downstream of a line source in turbulent channel flow. *Advances in Turbulence XI, Proceedings of the 11th EUROMECH European Turbulence Conference*, vol. 117, pp. 500–502.

Obukhov, A. M. 1949 Structure of the temperature field in a turbulent current. *Izv. Akad. Nauk SSSR Ser. Geogr. Geofiz* **13**, 58–69.

Paranthoën, P., Fouari, A., Dupont, A. & Lecordier, J. C. 1988 Dispersion measurements in turbulent flows (boundary layer and plane jet). *Intl J. Heat Mass Transfer* **31**, 153–165.

Pope, S. B. & Ching, E. S. C. 1993 Stationary probability density functions: an exact result. *Phys. Fluids* **5**, 1529–1531.

Prasad, R. R. & Sreenivasan, K. R. 1990 Quantitative three-dimensional imaging and the structure of passive scalar fields in fully turbulent flows. *J. Fluid Mech.* **216**, 1–34.

Raupach, M. R. & Legg, B. J. 1983 Turbulent dispersion from an elevated line source: measurements of wind-concentration moments and budgets. *J. Fluid Mech.* **136**, 111–137.

Rosset, L., Paranthoën, P., Lecordier, J. C. & Gonzalez, M. 2001 Anisotropy of a thermal field at dissipative scales in the case of small-scale injection. *Phys. Fluids* **13**, 3729–3737.

Schumacher, J. & Sreenivasan, K. R. 2005 Statistics and geometry of passive scalars in turbulence. *Phys. Fluids* **17**, 1–9.

Schumacher, J., Sreenivasan, K. R. & Yeung, P. K. 2005 Very fine structures in scalar mixing. *J. Fluid Mech.* **531**, 113–122.

Schwertfirm, F. & Manhart, M. 2007 DNS of passive scalar transport in turbulent channel flow at high Schmidt numbers. *Intl J. Heat Fluid Flow* **28**, 1204–1214.

Simens, M. P., Jiménez, J., Hoyas, S. & Mizuno, Y. 2009 A high-resolution code for turbulent boundary layers. *J. Comput. Phys.* **228**, 4218–4231.

Sinai, Y. G. & Yakhot, V. 1989 Limiting probability distributions of a passive scalar in a random velocity field. *Phys. Rev. Lett.* **63**, 1962–1964.

Sreenivasan, K. R. 1984 On the scaling of the turbulence energy dissipation rate. *Phys. Fluids* **27**, 1048–1051.

Sreenivasan, K. R. 1991 On local isotropy of passive scalars in turbulent shear flows. *Proc. R. Soc. Lond.* A **434**, 165–182.

Sreenivasan, K. R., Antonia, R. A. & Danh, H. Q. 1977 Temperature dissipation fluctuations in a turbulent boundary layer. *Phys. Fluids* **20**, 1238–1249.

STAPOUNTZIS, H., SAWFORD, B. L., HUNT, J. C. R. & BRITTER, R. E. 1986 Structure of the temperature field downwind of a line source in grid turbulence. *J. Fluid Mech.* **165**, 401–424.

SU, L. K. & CLEMENS, N. T. 2003 The structure of fine-scale scalar mixing in gas-phase planar turbulent jets. *J. Fluid Mech.* **488**, 1–29.

SUTTON, J. A. & DRISCOLL, J. F. 2013 Measurements and statistics of mixture fraction and scalar dissipation rates in turbulent non-premixed jet flames. *Combust. Flame* **160**, 1767–1778.

TAYLOR, G. I. 1935 Statistical theory of turbulence. Parts 1–4. *Proc. R. Soc. Lond.* A **151**, 421–478.

TENNEKES, H. & LUMLEY, J. L. 1972 *A First Course in Turbulence*. MIT Press, Cambridge, MA.

THOMSON, D. J. 1996 The second-order moment structure of dispersing plumes and puffs. *J. Fluid Mech.* **320**, 305–329.

THORODDSEN, S. T. & VAN ATTA, C. W. 1996 Experiments on density-gradient anisotropies and scalar dissipation of turbulence in a stably stratified fluid. *J. Fluid Mech.* **322**, 383–409.

TONG, C. & WARHAFT, Z. 1995 Passive scalar dispersion and mixing in a turbulent jet. *J. Fluid Mech.* **292**, 1–38.

UBEROI, M. S. & CORRSIN, S. 1952 Diffusion of heat from a line source in isotropic turbulence *Tech. Rep.* Nat. Adv. Comm. Aero.

VAN ATTA, C. 1991 Local isotropy of the smallest scales of turbulent scalar and velocity fields. *Proc. R. Soc. Lond.* A **434**, 139–147.

VRIELING, A. J. & NIEUWSTADT, F. T. M. 2003 Turbulent dispersion from nearby point sources – interference of the concentration statistics. *Atmos. Environ.* **37**, 4493–4506.

WARHAFT, Z. 1984 The interference of thermal fields from line sources in grid turbulence. *J. Fluid Mech.* **144**, 363–387.

WARHAFT, Z. 2000 Passive scalars in turbulent flows. *Annu. Rev. Fluid Mech.* **32**, 203–240.

WYNGAARD, J. C. 1969 Spatial resolution of the vorticity meter and other hot-wire arrays. *J. Phys. E: Sci. Instrum.* **2**, 983–987.

YEUNG, P. K., XU, S. & SREENIVASAN, K. R. 2002 Schmidt number effects on turbulent transport with uniform mean scalar gradient. *Phys. Fluids* **14**, 4178–4191.

ZHOU, T., ANTONIA, R. A., LASSERRE, J. J., COANTIC, M. & ANSELMET, F. 2003 Transverse velocity and temperature derivative measurements in grid turbulence. *Exp. Fluids* **34**, 449–459.